Preprint typeset in JINST style - HYPER VERSION

CALICE Analysis Note CAN-044, LCD-Note-2013-002
August 23, 2013

Shower development of particles with momenta from 10 to 100 GeV in the CALICE Scintillator-Tungsten HCAL

The CALICE Collaboration*

This note contains preliminary CALICE results, and is for the use of members of the CALICE Collaboration and others to whom permission has been given.

ABSTRACT: We present a study of the showers initiated by high momentum ($10 \leq p_{\text{beam}} \leq 100$ GeV) electrons, pions and protons in the highly granular CALICE analogue scintillator-tungsten hadronic calorimeter. The data were taken at the CERN SPS in 2011. The analysis includes measurements of the calorimeter response to each particle type and studies of the longitudinal and radial shower development. The results are compared to several GEANT4 simulation models.

*Corresponding author: A. Lucaci-Timoce (angela.isabela.lucaci.timoce@cern.ch)

Contents

1. Introduction

This paper presents the analysis of the data obtained with the CALICE analog hadronic calorimeter AHCAL [1] prototype at the CERN SPS in summer and autumn 2011 of mixed runs containing electrons, pions, protons, muons, and kaons with a momentum range of 10 to 300 GeV[1]. The present study is restricted to runs with an energy up to 100 GeV. This is due to the fact that with increasing energies, an increasing fraction of the shower energy leaks into the Tail Catcher and Muon Tracker (TCMT), while this analysis concentrates on events contained in the W-AHCAL.

The calorimeter was equipped with 38 tungsten absorber plates (W-AHCAL). Particles are identified using Cherenkov threshold counters and additional information based on the calorimeter high granularity.

General information about the W-AHCAL is given in [2]. More details about the absorber structure, about the beam-line instrumentation and the data taking conditions can be found in [3].

The purpose of the analysis is the comparison of data with the GEANT4 [4] simulation models in order to be able to judge on the reliability of the models relevant for the Monte Carlo studies done for detectors at the Compact Linear Collider (CLIC) [5].

2. Monte Carlo simulation and digitisation

A schematic representation of the CERN 2011 test beam line as implemented in the GEANT4 based simulation framework called Mokka [6] is shown in Fig. 1. The positions of the test beam elements were measured in a dedicated survey [7]. The centre of the W-AHCAL detector is placed at $x = -13.2$ mm and $y = 17.2$ mm.

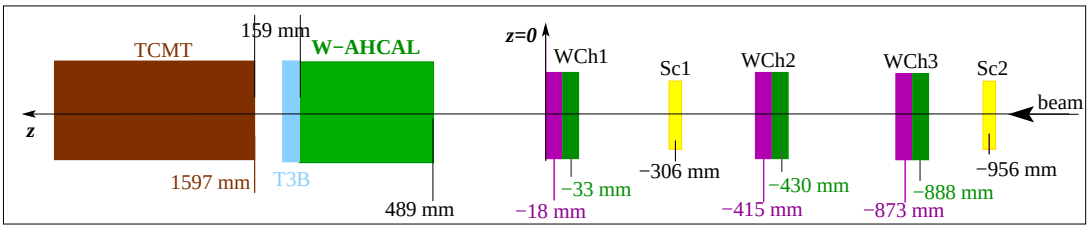

Figure 1: Sketch of the CERN 2011 test beam line as implemented in the Mokka model `TBCern2011WAHCAL` *(not to scale), where Sc stands for scintillator and WCh for wire chamber. The beam enters from right.*

In addition to the W-AHCAL, the following elements present in the SPS test beam are implemented in the simulation: two scintillators, three wire chambers, the T3B layer [8] and the Tail Catcher and Muon Tracker (TCMT) [9].

Particles of a given type and energy are generated using the particle gun, which is placed at $z = -50$ m. Interactions are modelled using the QGSP_BERT_HP, FTFP_BERT_HP[2] and the QGSP_BIC_HP physics lists, GEANT4 version 9.5.p01. These lists are described for example in [2].

In order to verify that no spurious effects are present in the simulation, the dependence of muon energy deposition in the scintillator tiles on the used GEANT4 version was studied. Moreover, the dependence on muon energy in the range from 10 to 100 GeV was investigated. In both cases, variations of the muon deposited energy of less than 1% were found [10, Appendix A.2].

To emulate the signal shaping time of the readout electronics in the Monte Carlo, only hits generated within a time window of 150 ns [11, pg. 57] are accepted. In addition, saturation effects in plastic scintillators described by Birks law are applied. For digitisation, a MIP to GeV factor of 805 keV and a cross-talk factor of 8% were used [2, pg. 39]. For each analysed run, 50000 Monte Carlo events are generated. They are digitised and reconstructed using the CALICE software version v04-06.

[1] In this paper, the natural system of units with $\hbar = c = 1$ is used.

[2] The FTFP_BERT_HP physics list is not included in the used GEANT4 version release, but we received it from the developers.

3. Calibration and temperature correction

The responses of all calorimeter cells are equalised to a common physics signal based on minimum ionising particles (MIPs), for which dedicated muon runs are used. Several steps are necessary to translate signals measured with the SiPM readout (in ADC counts) to information about the deposited energy (in MIPs).

The calibration of a single cell i is done according to:

$$E_i[\text{MIPs}] = \frac{A_i[\text{ADC}]}{A_i^{\text{MIP}}[\text{ADC}]} \cdot f_{\text{resp}}(A_i[\text{pixels}]), \tag{3.1}$$

where:

- $A_i[\text{ADC}]$ is the amplitude registered in cell i, in units of ADC counts;
- $A_i^{\text{MIP}}[\text{ADC}]$ is the MIP amplitude in cell i, measured also in ADC counts;
- $f_{\text{resp}}(A_i[\text{pixels}])$ is the SiPM response function which corrects for the non-linearity of the SiPM response that is due to the limited number of pixels (1156) and to the finite pixel recovery time ($20-500$ ns). This function acts on the amplitude expressed in number of pixels, and returns the saturation correction factor which needs to be applied to linearise the amplitude in MIPs.

  The response of all SiPMs was measured before mounting the sensors on the scintillator tiles. Due to geometrical effects, it is expected that the number of pixels which can detect light is reduced once the SiPMs are mounted on the tiles. To take this into account, the number of pixels from the response function is scaled with a factor s. An average value of $s = 0.8$ was measured for this scaling factor using CERN 2007 data, and is used in the calibration of the data analysed in this paper.

  The amplitude in pixels is obtained by dividing the amplitude of a cell by the corresponding SiPM gain $G_i[\text{ADC}]$:

$$A_i[\text{pixels}] = \frac{A_i[\text{ADC}]}{G_i[\text{ADC}]}. \tag{3.2}$$

  The gain values are obtained from fits of photo-electron spectra taken with low intensity LED light provided by a calibration and monitoring LED system.

Detailed information about the calibration procedure can be found in [12].

3.1 MIP calibration

The W-AHCAL response is calibrated to the response of muons, which are considered to be minimum ionising particles. For this, dedicated muon runs from September 2011 are used. For the MIP calibration, only runs are considered which have a small (26.9 ± 0.5°C) variation of the average temperature of the calorimeter.

In order to measure the MIP calibration factors, a track finding algorithm is used to reconstruct the muon track. Each active cell (i.e., a cell with an energy deposition above the threshold) is considered as seed, and it is checked if there are active neighbouring cells. A neighbouring cell is defined as the cell which is either directly or diagonally adjacent to the seed cell in the $(x,\ y)$ plane, and not further than 1 or 2 layers in the z-direction. If such a neighbouring cell is found, it is added to the track. In the next step, muon tracks with fewer than 8 active cells (i.e., hits) are rejected.

Input to the track finding algorithm is a file with hits which have the energy in units of ADC counts. For technical reasons, this energy is also saved in units of MIPs, using a set of calibrations from the CERN 2007 run period, such that a threshold cut of 0.3 MIPs can be applied before the algorithm is run. This is done for reasons of speed and of disk space.

Finally, for each cell with muon hits, the energy distribution is saved in a ROOT [13] histogram. These distributions are then fitted with a Landau function convolved with a Gaussian to obtain the so-called **MIP calibration factors**, A_i^{MIP} [ADC] (cf. equation 3.1), which are the most probable value of the energy deposition of a muon in a given cell, expressed in ADC counts.

3.2 MIP temperature correction

The temperature inside the calorimeter is measured using 5 sensors per layer. Details about the temperature measurements are given in [14]. In most of the layers the sensors are vertically aligned, which might be considered not optimal, as one could expect to also have temperature variations from the left to the right of a calorimeter layer. However, dedicated studies for a given detector layer found horizontal temperature variations of less than 0.5° Celsius [15].

Assuming an inverse linear dependence of the SiPM response on temperature, the MIP calibration factor of a given cell i is corrected for temperature variations using the formula:

$$A_i^{\mathrm{MIP}}[\mathrm{ADC}] = A_{i,T_0}^{\mathrm{MIP}}[\mathrm{ADC}] + (T_{\mathrm{run}} - T_0) \cdot slope, \tag{3.3}$$

where:

- $A_i^{\mathrm{MIP}}[\mathrm{ADC}]$ is the MIP amplitude in cell i, measured in ADC channels, and corrected for temperature;
- $A_{i,T_0}^{\mathrm{MIP}}[\mathrm{ADC}]$ is the MIP amplitudie in cell i, in ADC counts, obtained at the temperature T_0, i.e., at the average temperature during the muon runs of the sensor closest to the cell;
- T_{run} is the temperature of the sensor closest to the given cell, in the given run;
- $slope$ is the MIP slope determined for the layer of the given cell.

Because there is not enough statistics to measure the MIP temperature slopes per channel, so-called MIP relative slopes are measured for each calorimeter layer, using the method described in [2]. These slopes, expressed in percents of MIPs per degree Celsius, are measured relative to the calorimeter response obtained at the temperature at which the muon calibration runs were taken.

For 4 calorimeter layers (22, 26, 27 and 28), no reliable slopes could be determined. For these specific layers, the average of all the other slopes is used. The average relative slope considering all layers is $-4.5\%/^{\circ}\mathrm{C}$ before the temperature correction, and better than $0.06\%/^{\circ}\mathrm{C}$ after.

4. Statistical and systematic uncertainties

The measurements of the calibration factors comprise two types of uncertainties: a statistical uncertainty of the measurement itself and a systematic uncertainty associated to the measurement method.

The statistical uncertainties are uncorrelated between the different channels. Thus one can assume that for a large number of channels (a few hundred), these uncertainties are significantly reduced. This holds for the gain and inter-calibration factors, since in these cases all channels are measured in parallel.

In the case of the MIP calibration, the muon traverses only one (or two) cells of each calorimeter layer per event. To ensure the quality of the MIP calibration factors, only MIP factors with a relative statistical uncertainty smaller than 2% are accepted, as shown in Fig. 2. This way only fits with high statistics are considered, as indicated in Fig. 3.

Possible sources of systematic uncertainties due to MIP calibration factors, MIP and gain temperature slopes, the noise measurement, applied voltages, the scaling factor of the SiPM response curve, the stability of the detector response in time, and the time cut in the simulation are discussed in the following.

4.1 MIP calibration factors

In [12, pg. 12] a MIP systematic uncertainty of 2%, due to imperfections of the parametrisation of the MIP line shape and other effects like binning or bias in the muon track selection, was found. This uncertainty affects all channels in the same way.

The statistical uncertainty of the channel-wise calibration can be extracted from the width of the distribution of the differences between the result of independent calibration periods from July and September 2011.

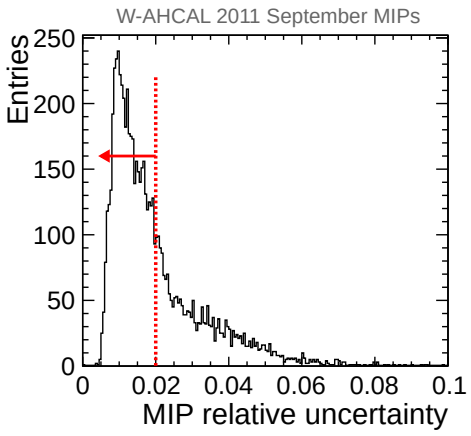

Figure 2: Distribution of MIP relative statistical uncertainties for 2011 September calibrations. The line and the arrow indicate the selection cut, i.e., only calibration factors with a relative uncertainty smaller than 2% are accepted.

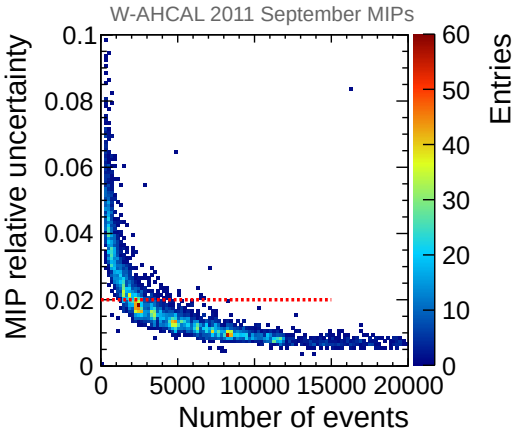

Figure 3: Dependence of the MIP relative statistical uncertainties for 2011 September calibrations on the number of events. The line indicates the selection cut, i.e., only calibration factors with a relative uncertainty smaller than 2% are accepted.

Table 1: Summary of uncertainties for the energy sum per calorimeter and per layer due to the MIP calibration factors.

Measurement	Source	Total	Comments
Total energy sum	2% from correlated systematic uncertainties	$\pm 2\%$	
Energy sum per layer	2% from correlated systematic uncertainties and 2.6% from uncorrelated statistical uncertainties	$\pm 3.6\%$	Added in quadrature due to independent origins

This yields an uncertainty of $0.0369/\sqrt{2} = 2.6\%$, which is uncorrelated from one channel to the other[3]. This uncertainty has a negligible impact on the total energy sum, because the effect is reduced by a factor $\sqrt{N}$, where N is the number of cells contributing to the measurement. However, this uncertainty will affect the longitudinal shower profiles, because an individual layer can be dominated by a few cells only, as in the case of electromagnetic showers.

The uncertainties due to the MIP calibration factors are summarised in Table 1.

4.2 MIP and gain temperature slopes

The MIP calibration factors are corrected for temperature variations using equation 3.3. The MIP temperature slopes are obtained with a linear fit. The average relative error of the MIP temperature slopes, using September 2011 muon runs, is 2.3%. Varying up and down the slopes according to this uncertainty resulted in a negligible change in the average total energy sum.

Similar to the MIP calibration factors, the gain factors are also corrected for temperature variations. However, the gain enters in the calibration formula only indirectly, via the response function (equations. 3.1 and 3.2). In addition, the gain temperature dependence is smaller than the MIP temperature dependence ($-1.7\%/^{\circ}$C compared to $-4.5\%/^{\circ}$C), therefore it is expected that the uncertainty on the temperature slope has a smaller effect in this case.

[3]This uncertainty includes the uncorrelated channel to channel variations of the temperature coefficient, which is significant, since we use a representative average per layer. So it can be larger than the statistical error extracted from the MIP fit.

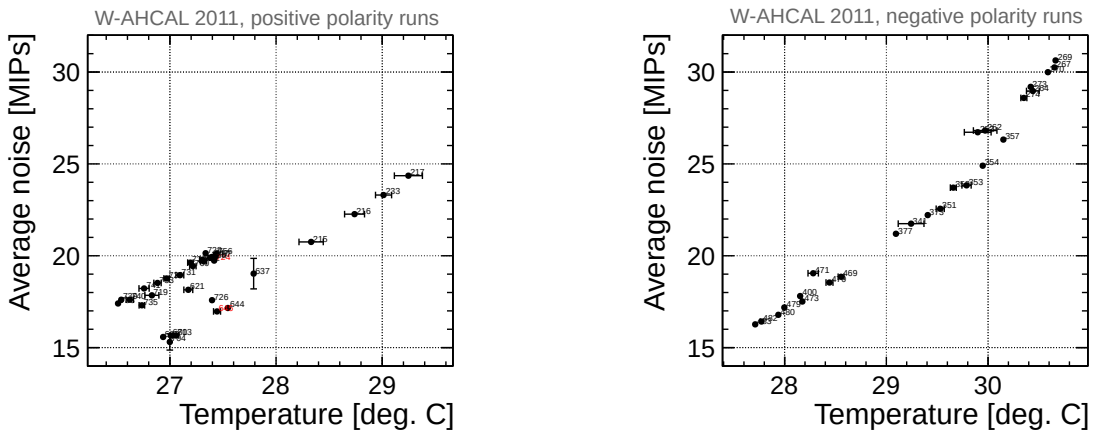

Figure 4: Dependence of the W-AHCAL average noise on temperature, for positive (left) and negative (right) polarity runs. The numbers indicate the run number minus 361000.

4.3 Noise measurement

In order to monitor the noise level in the calorimeter, every 35000 events, 500 events are taken with random triggers. During reconstruction, the average pedestal baseline is subtracted for each channel.

The distribution of the total energy sum in random trigger events, due to noise hits above threshold, is approximately Gaussian. Its mean value depends on temperature, as can be seen in Fig. 4. In the following, unless otherwise stated, noise is not subtracted from the data. It is accounted for by superimposing random trigger events from the relevant run period to the simulation.

For some positive polarity runs, there are additional fluctuations of the noise, which are not temperature induced, but which are negligible with respect to the energies deposited by particles. We therefore do not assign a systematic uncertainty associated with the noise treatment.

4.4 Applied voltages

Since the gain depends linearly on both voltage and temperature, a change in the bias voltage at a fixed temperature corresponds to a certain temperature change at a fixed bias voltage.

The bias voltages applied in the W-AHCAL during the 2011 data taking are stable for most of the runs, the maximum variations of about 20 mV are observed only in a few cases. Nevertheless, the impact of these variations is negligible, compared to the breakdown-voltage temperature dependence[4] of 56 mV/K [16, pg. 16].

4.5 Scaling factor of the SiPM response curves

As discussed in section 3, the response curves for each SiPM were measured before mounting the sensors on the scintillator tiles [12, pg. 7]. Due to geometric effects, the maximum number of pixels for mounted SiPMs is on average 80% of the value measured for bare SiPMs, with a wide distribution (RMS $= 9\%$, where RMS is the root mean square). For this reason, the response curves of all AHCAL channels are scaled with a factor $s = 0.8$.

In the case of electromagnetic showers in the W-AHCAL, due to the dense absorber (corresponding to about 3 radiation lengths X_0 per layer), most of the energy is deposited in a few cells in the first calorimeter layers. An example is shown in Fig. 5 for 40 GeV e^+. Since more than half of the energy in a layer belongs to a single cell, uncertainties in the scaling factor are expected to have significant effects.

To estimate the systematic uncertainties due to the scaling factor, we re-run the reconstruction of the data using two different values of this factor for the one cell with the highest energy in layer 2: $s = 0.71$ (-1 RMS), and $s = 0.89$ ($+1$ RMS). The impact is shown for 15 and 40 GeV e^+ in the case of of the total energy sum in Fig. 6. The systematic uncertainties due to the scaling factors are obtained by comparing the average visible energy measured in data reconstructed using the different scaling factors. The average energy is given by the

[4]The SiPM response depends on the over-voltage $\Delta V = V_{\text{bias}} - V_{\text{breakdown}}$ and is sensitive to changes of V_{bias} in the same way as to temperature-induced changes of $V_{\text{breakdown}}$.

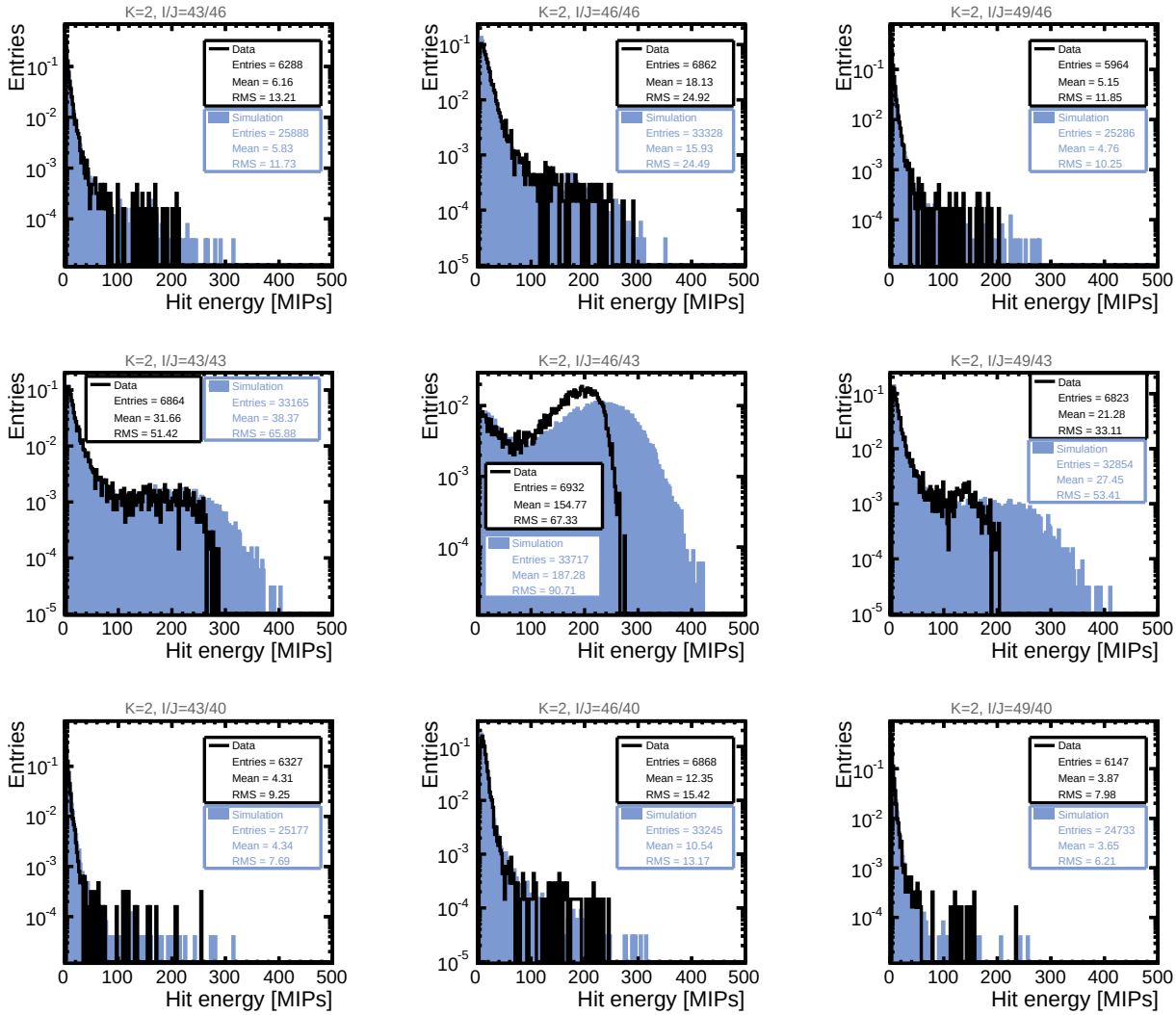

Figure 5: Hit energy distributions for 40 GeV e^+. The central cells of layer 2 are shown. Data are compared to the simulation. About 60% of the total energy in the layer is deposited in one cell. The corresponding distribution is shown in the middle of the figure.

Table 2: Average energy deposited by e^+. Data reconstructed using different scaling factors for the highest energy cell in the calorimeter layer 2 are compared.

p_{beam} (GeV)	$s = 0.8$ (default)	$s = 0.71$ (-1 RMS)	$s = 0.89$ ($+1$ RMS)
15	439 MIPs	+1.0%	−0.5%
20	585 MIPs	+1.7%	−0.3%
30	890 MIPs	+2.7%	−1.7%
40	1186 MIPs	+3.0%	−2.0%

mean of an iterative fit with the Novosibirsk function [2, pg. 13] in the a central region defined by $mean \pm 1.5\ \sigma$. An example fit is shown in Fig. 7 for 15 GeV e^+. The results for the analysed e^+ energies are given in Table 2.

In the case of longitudinal profiles, the effect due to the scaling factor uncertainties is larger, due the fact that only a small number of cells per layer contribute to the signal. This was estimated by comparing the energies in layer 2, since this is the layer of the cell for which the scaling factor was modified. An example of longitudinal profile corresponding to the different scaling factors is shown in Fig. 8 for 40 GeV e^+. The obtained results are indicated in Table 3. The variations observed in layer 2 are used as a conservative estimate for the relative variations in the other layers, although there the effects are expected to be smaller, due to the smaller amplitudes.

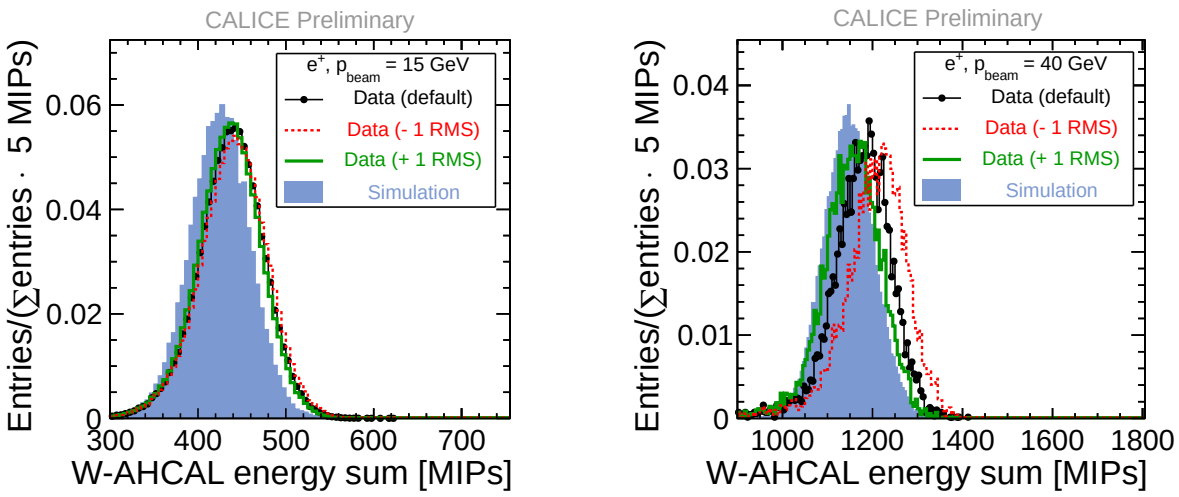

Figure 6: Distributions of the energy sum over all cells for 15 GeV e^+ (left) and 40 GeV e^+ (right). The data are reconstructed with a varying saturation scaling factor of $s = 0.8 \pm 1 \cdot RMS$ for the highest energy cell in the calorimeter layer 2 and compared with the simulation.

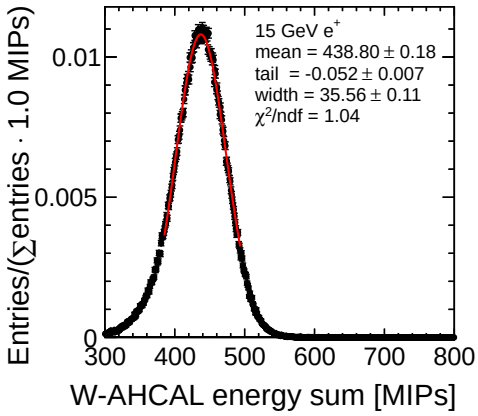

Figure 7: Fit of the energy sum distribution of 15 GeV e^+ with the Novosibirsk function. The obtained fit parameters are also indicated.

Due to the dense showers in tungsten, the uncertainties related to saturation corrections limit the precision with which we can validate the detector simulation and calibration using high energy electron data.

4.6 Cross-talk factor

Due to the imperfect reflective coating of the scintillator tiles, light may leak between neighbouring calorimeter cells. This is taken into consideration in the simulation via the so-called cross-talk factor, which is the fraction of energy which leaks into neighbouring cells. Measurements of the cross-talk found values of 2.5% [12, pg. 10], and between 3.3% and 4.6% of the total energy per edge for the 3×3 cm^2 cells [17].

In the simulation, the cross-talk factor is relevant as it sets the energy scale: the higher this factor, the higher the final energy is. To account for the imperfect knowledge of the cross-talk, and hence of the energy scale, an uncertainty of 5% is assumed conservatively for the total energy sum.

As the cross-talk affects the energy deposited in the radial plane, one might expect to have an impact on the radial profiles. This was studied for 25 and 100 GeV π^+ events, using a cross-talk factor twice the default used in the analysis, i.e., of 4% per tile edge [2, Appendix B]. This had only a minor impact on the shape of the radial profiles.

4.7 Selection purities

The analysed data contain mixed pion, proton, kaon, electron, and muon events. Events from a given particle

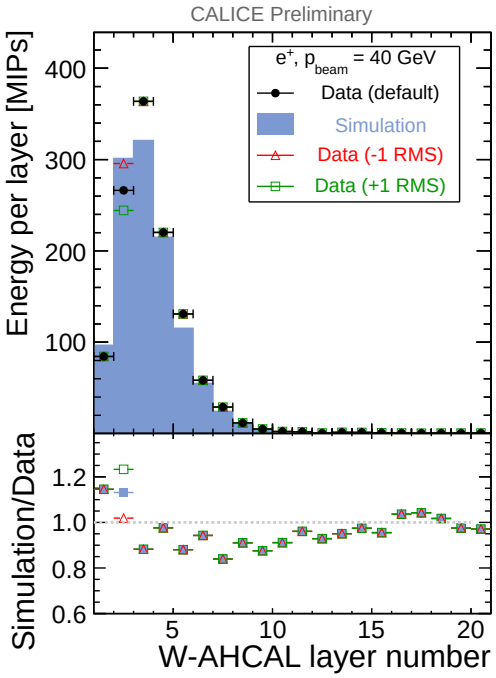

Figure 8: Longitudinal profile for 40 GeV e^+. Data reconstructed with the different scaling factors are compared to the simulation.

Table 3: Change in the energy deposited by e^+ in the W-AHCAL layer 2. Data reconstructed using different scaling factors are compared.

p_{beam} (GeV)	$s = 0.8$ (default)	$s = 0.71$ (-1 RMS)	$s = 0.89$ ($+1$ RMS)
15	127 MIPs	+1.7%	−2.5%
20	160 MIPs	+2.6%	−4.8%
30	219 MIPs	+6.4%	−8.6%
40	265 MIPs	+9.0%	−10.0%

type are selected using Cherenkov threshold counters and information based on shower shapes. While the electron and muon contamination is efficiently reduced by using calorimeter information, the distinction between pions, kaons and protons is solely based on Cherenkov counters. The purity of the selected hadron samples was determined in [18]. For this analysis, only runs which have a purity better than 80% for a given hadron type are considered.

It would be possible to estimate the systematic uncertainties due to the remaining contamination from other hadrons by comparing the differences in the shower shapes in Monte Carlo. However, as it will be shown later, the CALICE W-AHCAL has a very similar response for all analysed hadron types in the energy range from 10 to 100 GeV. Therefore no systematic uncertainties due to possible contaminations are considered.

4.8 Stability of the detector response in time

To check the stability of the detector response in time, we studied the variation of the average hadronic energy sum deposited in the calorimeter (i.e., visible energy), divided by the corresponding beam momenta, as a function of the run number. The data selection is discussed in Section 6. The average energy is obtained with a Gaussian fit as exemplified in Fig. 9.

The obtained time dependence is shown in Figs. 10. This variation cannot be explained by temperature effects, as these are corrected for [10, Appendix A.8.]. While the response to protons seems to be stable, variations with an RMS of 3.1% are observed for π^- and π^+. This is not understood, especially because the proton and π^+ events are selected from the same positive polarity runs. These variations also cannot be explained by the usage of secondary and tertiary beams. As visible in Fig. 11, the differences observed in the mean energy sum from runs taken with different beam types is less than 1%.

Negative polarity runs give on average a higher response (up to 5%) than positive polarity runs. This holds also for the $e^{\pm}$ data (Section 5.2).

The systematic uncertainties due to the observed variations of the calorimeter response are quantified by the ratio between the RMS and the mean of the distributions of the ratio between the average visible energy and the beam momenta, and are given in Table 4.

The stability of the calorimeter response was also investigated for muons in hadron runs. The ratio between the average hit energy of muons from negative and positive polarity runs is shown as a function of the calorimeter

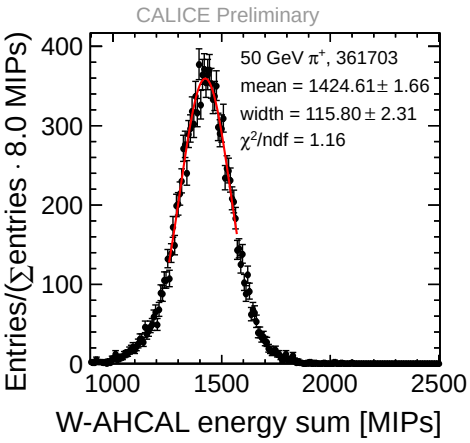

Figure 9: Distribution of the W-AHCAL energy sum for 50 GeV π^+, run 361703. The red line indicates a Gaussian fit in a central region containing 80% of the statistics.

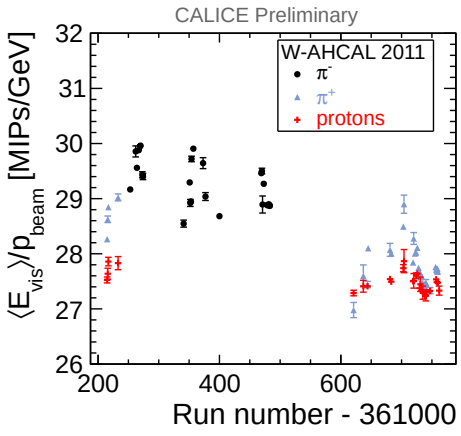

Figure 10: The ratio between the average visible energy and the beam momenta for $\pi^{\pm}$ and protons as a function of the run number minus 361000. Each marker corresponds to one run. The mean noise above threshold is subtracted from the average energy.

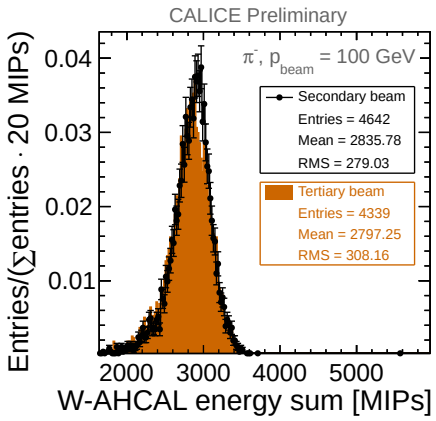

Figure 11: Energy sum distribution of 100 GeV π^-. Two runs taken with secondary and tertiary beams are compared.

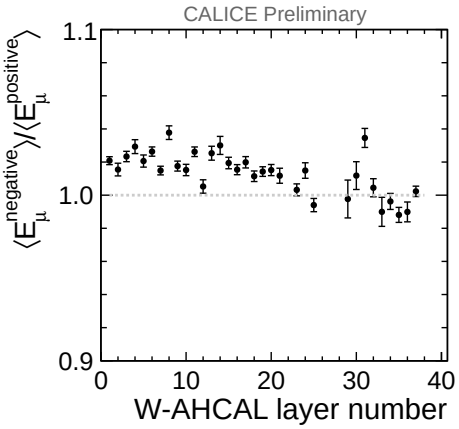

Figure 12: The ratio between the average hit energy of muons from negative and positive polarity runs as a function of the calorimeter layer number. In layers 22, 26, 27 and 28 no muon peak was visible.

Table 4: Ratio between the RMS and mean of the distributions of the ratio between the average visible energy and the beam momenta ($\langle E_{vis} \rangle / p_{beam}$) for $e^{\pm}$ and for hadron runs.

Particle type	RMS/Mean
$e^{\pm}$	2.0%
Hadrons	3.1%

layer in Fig. 12. The response of the first calorimeter layers is higher in the case of negative polarity runs, but the difference is within the systematic uncertainties of the calibration, and not sufficient to fully explain the variations observed for the pion data.

Concerning the different response of the W-AHCAL to particles of the same nominal momenta, one might at first suspect an issue with the true energy of the particles linked to the settings of the beam line elements. The H8 beam line is, basically, a spectrometer in which the particle momenta are defined by fixed collimators and one

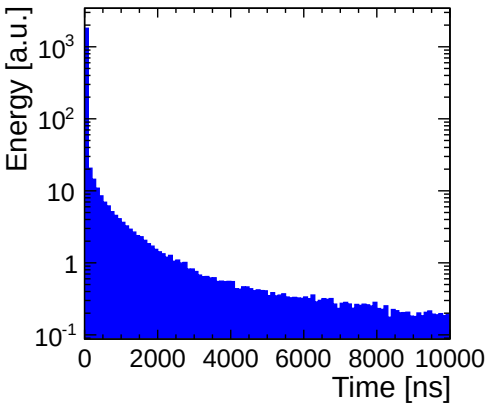

Figure 13: Dependence of the energy of 20 GeV π^+ hits, simulated with QGSP_BERT_HP, on the time of the hit.

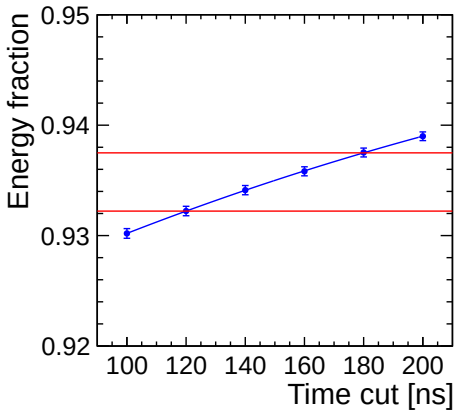

Figure 14: Dependence of the energy fraction of 20 GeV π^+ on the time cut applied in the simulation. The red lines indicate the variations of the energy fraction corresponding to $\pm$30 ns around the time cut of 150 ns applied in the simulation.

large spectrometer magnet (in fact, six deflection magnets connected in series of two pairs, called BEND3 and BEND4, are acting as the "spectrometer magnet" with a total deflection angle of about 41 mrad). The current I(BEND3)=I(BEND4) in these magnets together with the collimator settings defines the average momentum and momentum spread of the particles used by the H8 beam tests. For example, for a 40 GeV test beam, the current is I(BEND3)=I(BEND4)=125.8 A (the current is proportional to the chosen particle momentum for all but the highest H8 beam energies).

The current is set, and after some delay allowing for stabilisation, is read back by two independent Direct Current-Current Transformers (DCCTs) per magnet. The intrinsic accuracy of the DCCTs can be as good as 10^{-4}, however for practical reasons the control system aims at differences between set and read current of less than 0.2 A. The user gets an alarm (red line on the control screen) when the current read varies from the set current by 0.4 A or more.

For beam energies of 20 GeV and below, the de-magnetisation procedure prepared in the beam line control system has systematically been used during the W-AHCAL runs, in order to avoid the effects of remnant fields in the spectrometer magnet. (The contribution of the remnant fields in BEND3 and BEND4 without demagnetisation would correspond to a total error in the average beam momentum of about 0.1 GeV). In summary, one can conclude that the run-by-run particle momentum is defined by the H8 beam spectrometer to better than 1% at 40 GeV and above and (much) better than 2% at 10, 20 and 30 GeV. It is worth noting that, with much additional effort as e.g. for dedicated tests of electromagnetic calorimeters such as described in [19], a considerably better beam energy determination could be achieved, but this is generally not necessary for HCAL beam tests. We also note that, with all collimators of the H8 beam line fully opened, a beam momentum spread $\delta p/p$ of $\pm$2.1% in tertiary beam mode ($\pm$1.5% in secondary beam mode) is achieved. Magnet apertures prevent the transport of off-momentum particles beyond these limits.

4.9 Time cut in simulation

As explained in Section 2, a time cut of 150 ns is applied on simulated hits in order to emulate the signal shaping time of the CALICE readout electronics. For the Fe-AHCAL, it was found that changing the cut with the observed variations of 15 ns has very small effects (at the per mill level) on the reconstructed pion energy [11].

For the W-AHCAL case, tungsten is used as absorber, and a rather large fraction of the signal is produced by late spallation neutrons. While most of the energy is deposited within the first nanoseconds, there are also late energy deposits, as shown in Fig. 13 for the case of 20 GeV π^+, simulated with QGSP_BERT_HP. To estimate the effects due the time cut, variations of $\pm$30 ns were considered. In Fig. 14 the energy fraction (relative to the

total energy deposited when no time cut is applied) is shown as a function of the time cut. The red lines indicate the region corresponding to ± 30 ns around the time cut of 150 ns applied in the simulation, resulting in about $\pm 0.3\%$ variations of the measured energy in the simulation, which is negligible.

4.10 Summary of uncertainties

The systematic uncertainties assumed for the different calibration parameters, which are considered in the analysis of the experimental data, are summarised in Table 5. The total uncertainty is obtained by adding all the numbers in quadrature. For the Monte Carlo simulation, an uncertainty of $+5\%$ on the energy scale is assumed, which is due to the imprecise knowledge of the cross-talk factor.

The uncertainties due to gain and inter-calibration, MIP and temperature slopes, noise, voltages, and time cut in the simulation are negligible.

Table 5: Systematic uncertainties of the energy sum per calorimeter and per layer, which are considered in the analysis of the experimental data. For the e^+ data, only the 40 GeV case is indicated, as for this energy the systematic uncertainties are the highest. For the hadron data, the indicated uncertainties are valid for all analysed energies.

Particles	Measurement	Uncertainty	Total systematic uncertainty
40 GeV e^+	Total energy sum	$\pm 2.0\%$ (MIP scaling factor) $\pm 2.0\%$ (stability of detector response) $+3\%, -2.0\%$ (saturation scaling)	$+4.1\%, -3.5\%$
	Energy sum per layer	$\pm 2.0\%$ (MIP scaling factor) $\pm 2.0\%$ (stability of detector response) $+9\%, -10\%$ (saturation scaling)	$+9.4\%, -10.4\%$
Hadrons	Total energy sum	$\pm 2.0\%$ (MIP scaling factor) $\pm 3.1\%$ (stability of detector response) -0.5% (saturation scaling)	$\pm 3.7\%$

5. Analysis of the $e^{\pm}$ data

The list of $e^{\pm}$ runs is given in Appendix A.1. In addition to electron events, these runs contain also muons, and events in which the electron showered before the W-AHCAL. To increase the purity of the electromagnetic data, clusters are identified in 3-D using the nearest-neighbour algorithm developed in [11]. Using muon calibration runs, a threshold was set to distinguish energy deposits by single and multiple particles in a showers. The cells with energy above this threshold are used as seeds for clustering. All active cells which surround the seed cell and have an energy deposit above the threshold are added to the cluster.

5.1 Data selection

The $e^{\pm}$ events are selected if they fulfil the following requirements:

1. The number of identified clusters in the whole calorimeter is one: since tungsten is a dense absorber material, most of the electromagnetic showers will form a cluster in the first calorimeter layers (Fig. 15);

2. The centre-of-gravity in z of the identified cluster should be less than 650 mm, as indicated in Fig. 16 for 15 GeV e^+;

3. The events should not contain an identified track. Tracks are searched for using the algorithm developed in [20]. If there is a track, this belongs most probably to a muon.

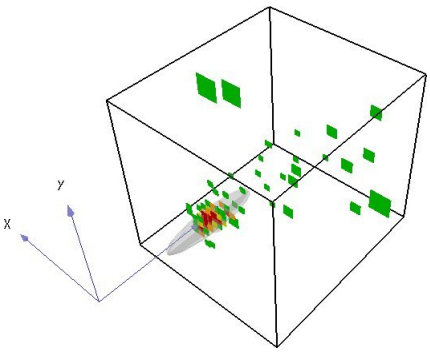

Figure 15: Display of a 15 GeV e^+ event. The ellipsoid shows the identified cluster. The colours of the W-AHCAL cells indicate the deposited energy, red being the highest (more than 5.4 MIPs).

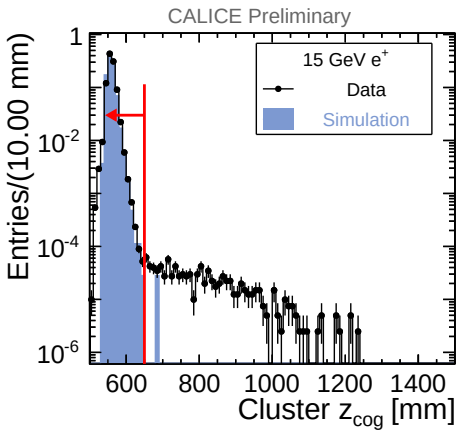

Figure 16: Distribution of the cluster centre-of-gravity in z (in the laboratory system) for 15 GeV e^+. The line indicates the selection cut.

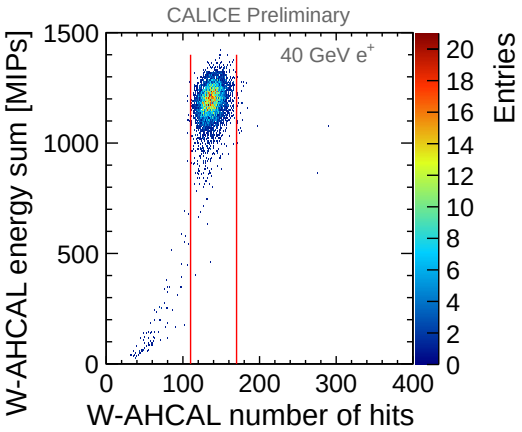

Figure 17: Distribution of the energy sum as a function of the number of hits in the W-AHCAL for 40 GeV e^+. The lines indicate the selection cuts.

Table 6: Cuts on the minimum and maximum number of hits applied for the $e^\pm$ selection.

p_{beam} [GeV]	$N_{\text{hits}}^{\text{min}}$	$N_{\text{hits}}^{\text{max}}$
10	65	105
15	75	110
20	80	120
30	95	140
40	110	170

4. The number of hits in the W-AHCAL should be inside a range[5] as defined in Table 6 and shown in Fig. 17. This is done in order to reject the few events in which the electrons shower already before entering the W-AHCAL.

To reduce the influence of noise in the $e^\pm$ events, the calorimeter hits are selected for subsequent analysis if they fulfil the following criteria: are contained within the first 20 calorimeter layers and within the 3×3 cm^2 tiles.

The distribution of the energy sum for 15 GeV e^+ after the different selection cuts is shown in Fig. 18, and in Fig. 19 for 40 GeV e^+. The corresponding accumulated reduction of the number of events are given in Table 7 for 15 GeV, and in Table 8 for 40 GeV e^+.

During data taking, it was observed that the distribution of the visible energy deposited by $e^\pm$ shows a long tail towards low energies. One assumption was that this was due to interactions with the beam line ma-

[5]The cuts on the number of hits are applied only for the experimental data, not for the simulation, in which no tails are observed.

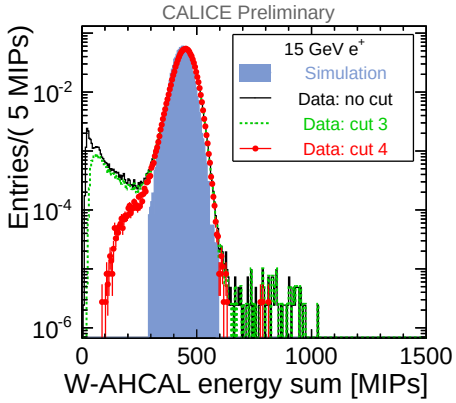

Figure 18: Energy sum distributions for 15 GeV e^+: the simulation, as well as the experimental data, after the different selection cuts, are shown.

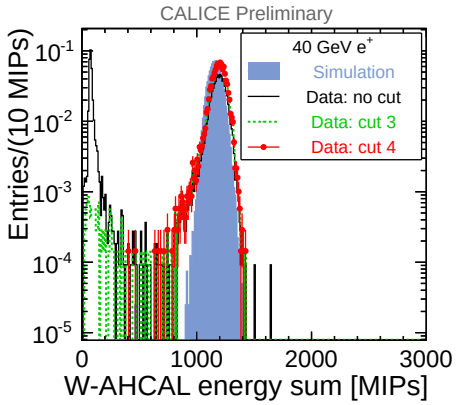

Figure 19: Energy sum distributions for 40 GeV e^+: the simulation, as well as the experimental data, after the different selection cuts, are shown.

Table 7: Selection cuts for 15 GeV e^+ and corresponding accumulated reduction of the number of events in data (with respect to the case in which no cut is applied).

Cut	Meaning	Reduction
1	$\#clusters = 1$	2%
2	& $z_{\mathrm{cog}}^{\mathrm{cluster}} < 650$ mm	2%
3	& $\#tracks = 0$	4%
4	& $\#hits > N_{\mathrm{hits}}^{\mathrm{min}}$ and $\#hits < N_{\mathrm{hits}}^{\mathrm{max}}$	10%

Table 8: Selection cuts for 40 GeV e^+ and corresponding accumulated reduction of the number of events in data (with respect to the case in which no cut is applied).

Cut	Meaning	Reduction
1	$\#clusters = 1$	22%
2	& $z_{\mathrm{cog}}^{\mathrm{cluster}} < 650$ mm	32%
3	& $\#tracks = 0$	34%
4	& $\#hits > N_{\mathrm{hits}}^{\mathrm{min}}$ and $\#hits < N_{\mathrm{hits}}^{\mathrm{max}}$	35%

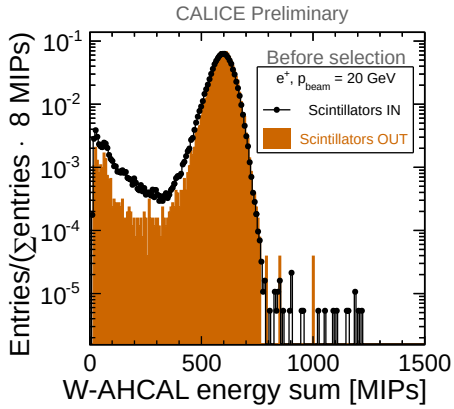

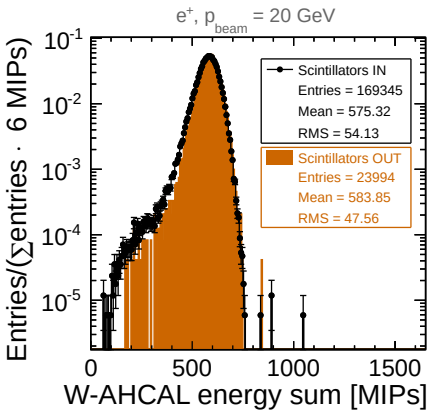

Figure 20: Energy sum distributions for 20 GeV e^+, before (left) and after selection (right). Two runs taken with and without beam line scintillators are compared.

terial. To test this hypothesis, several upstream scintillators (more than 50 m away from the calorimeter) were removed from the beam line. A comparison of the energy distribution for two runs taken with and without these scintillators is shown in Fig. 20. It appears that in the case where the scintillators were removed, the tail is reduced.

The data suggest that the low energy tail observed in the electron energy distribution is related to material in the beam line. However, this is not fully reproduced by the simulations, which include the materials known to be

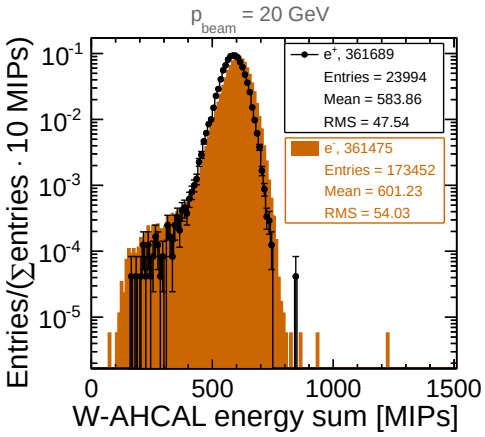

Figure 21: Energy sum distributions for 20 GeV $e^{\pm}$. Two runs taken without beam line scintillator are shown.

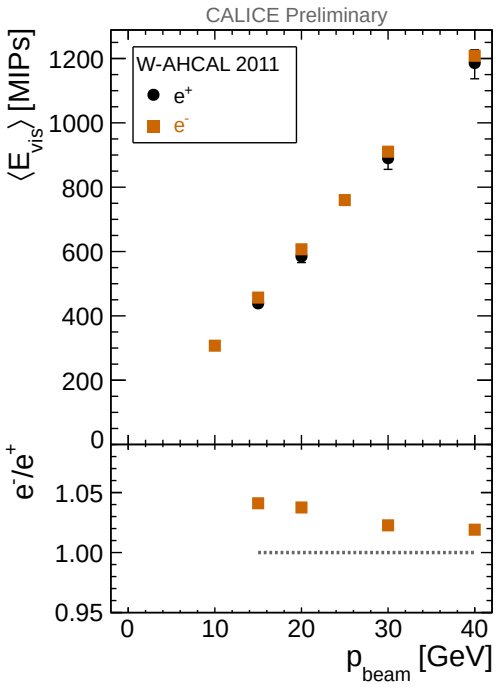

Figure 22: Average $e^{\pm}$ visible energy as a function of the beam momentum.

present in the installation. This somewhat limits the ability to model the electron longitudinal shower profiles, but it is not expected to significantly affect the hadron analyses.

5.2 Comparison of e^+ with e^- data

When comparing runs with negative and positive polarity, it was noticed that in e^- runs the calorimeter has a systematically higher response than in e^+ runs, by a few percent. This is shown in Figs. 21 and 22. The reason for this difference is unknown, but we note that the e^- and e^+ runs were taken at different times during 2011, with the detector being re-installed. As discussed in Section 4.8, we also observe a difference between the visible energy for π^- and π^+, but again the runs were taken at different times. (As expected, in the GEANT4 simulation the calorimeter response to e^- is the same as to e^+, and very similar between π^- and π^+.)

5.3 Comparison with simulation

The analysis of electromagnetic data in a hadronic calorimeter is important in view of a comparison with simulation. As the theory of electromagnetic showers is well known, a disagreement between data and Monte Carlo could be an indication of:

- Problems with the implementation of the detector material in the simulation;
- Calibration issues;
- Detector instabilities;
- Other unknown effects.

Regarding the implementation of the detector material in the simulation, the following checks were done:

- The Mokka model for 2011 gives the same response for electromagnetic data as the 2010 model, which was used in the analysis presented in [2], and which gave good agreement between data and Monte Carlo.
- The detectors implemented in the simulated test beam line, and their materials, were checked.

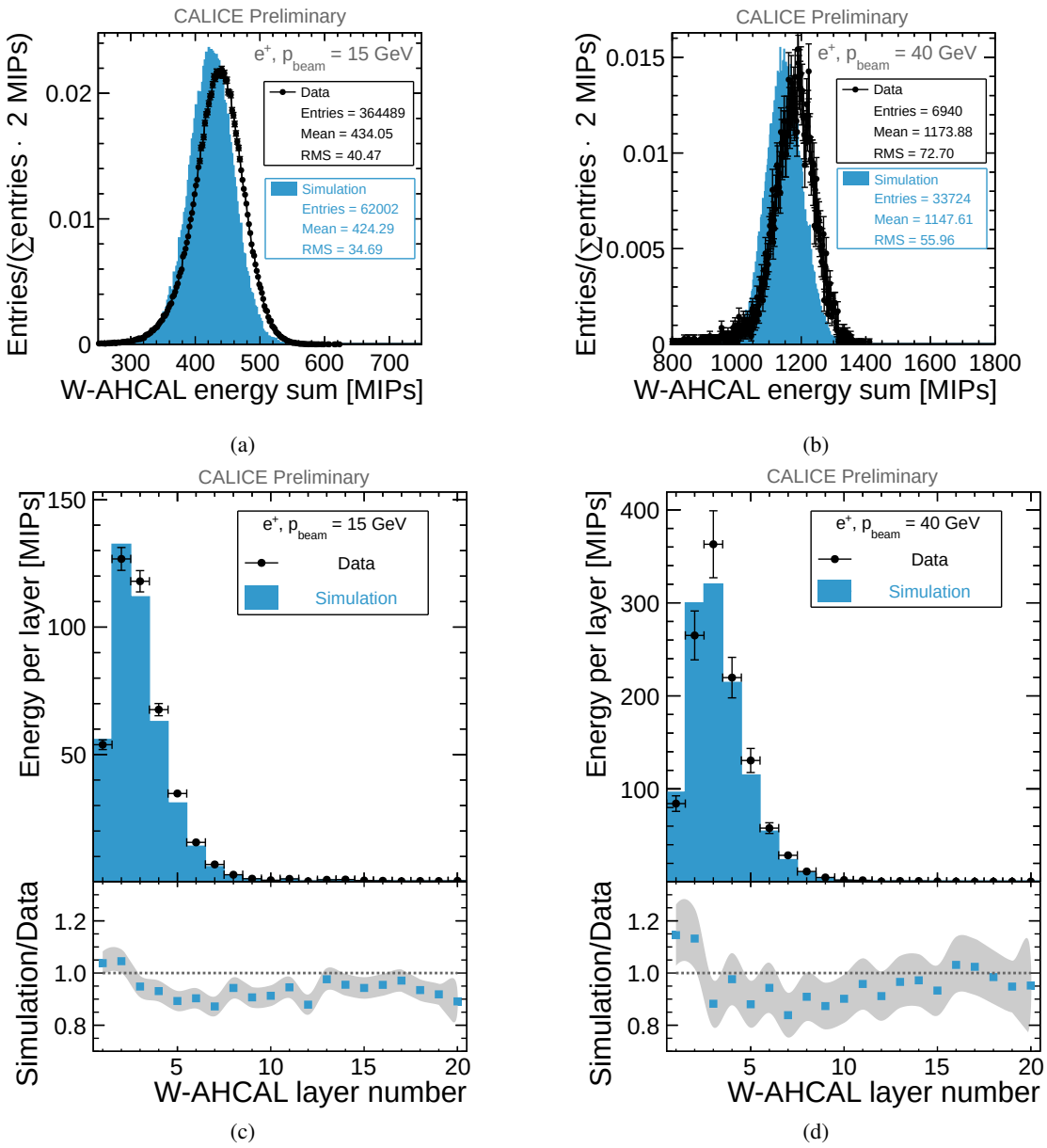

Figure 23: Comparison of 15 and 40 GeV e^+ data with simulation: energy sum distributions (a, b) and longitudinal profiles (c, d). The grey band shows the overall uncertainty.

For the comparison with Monte Carlo, only positron data are considered. Figure 23 shows the energy sum distributions and the longitudinal profiles (i.e., the distribution of the average energy deposited in a given calorimeter layer as a function of the layer number) for 15 and 40 GeV e^+. The reason of the observed disagreement is unclear, it might be due to detector instabilities or other unknown systematic effects.

In Fig. 24 the average e^+ visible energy and the width of the energy sum distributions, obtained with an iterative fit using the Novosibirsk function (cf. Fig. 7), are shown as a function of the beam momentum. The data are fitted with a linear function, and the fit results are given in Table 9. The statistical uncertainties (stat) are obtained directly from the fit. To estimate the systematic uncertainties (sys), the following procedure was followed:

- 100 experiments were run by varying the measured $\langle E_{vis} \rangle$ with a random Gaussian function with the mean equal to $\langle E_{vis} \rangle$, and with sigma given by $\langle E_{vis} \rangle \cdot \delta_{sys}$, where δ_{sys} is the average total systematic uncertainty for e^+, as indicated in Table 5;

- For each experiment, a linear fit is applied, and the values of the measured fit parameters are filled in separate histograms;

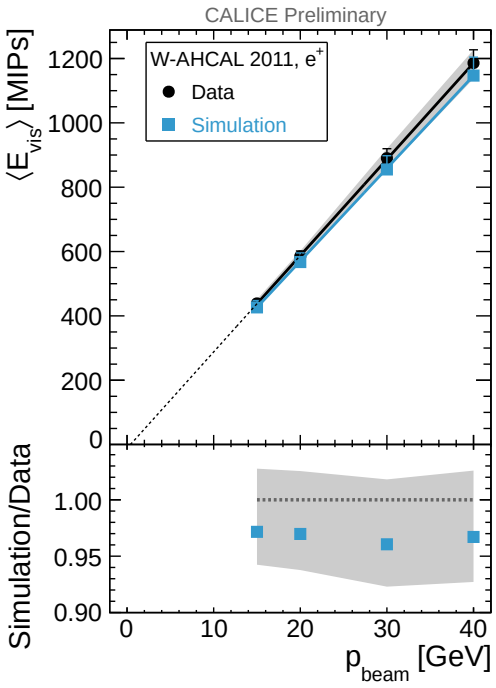

Figure 24: Dependence of the mean visible energy on the beam momenta for 2011 e^+ W-AHCAL data. The grey band shows the overall uncertainty. The lines indicate fits with the function $E_{vis} = u + v \cdot p_{beam}$.

Table 9: Fit parameters of the dependence of the mean visible energy on the beam momenta for the 2011 e^+ W-AHCAL data. Both statistical (stat) and systematic (sys) uncertainties are indicated for the fit parameters.

Parameter	Data
u [MIPs]	-11.77 ± 4.29 (stat) ± 75.80 (sys)
v [MIPs/GeV]	29.97 ± 0.15 (stat) ± 2.40 (sys)
Parameter	**Simulation**
u [MIPs]	-8.12 ± 3.45 (stat) ± 66.66 (sys)
v [MIPs/GeV]	28.84 ± 0.12 (stat) ± 1.15 (sys)

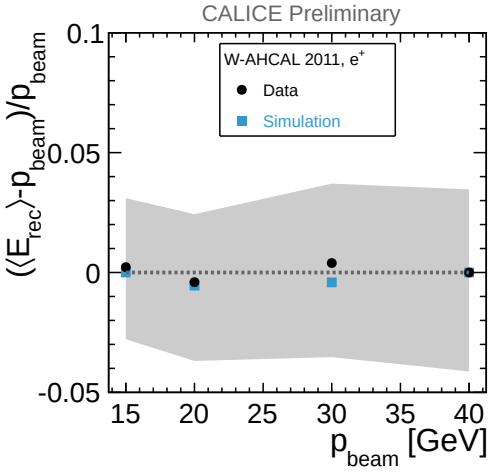

Figure 25: Deviation from linearity for the W-AHCAL 2011 e^+ data. The grey band shows the overall uncertainty.

- Then the systematic uncertainty is estimated as the one standard deviation of the corresponding histogram.

The slopes are similar for data and Monte Carlo (within the uncertainties), while large uncertainties are observed for the offsets, which are consistent with zero.

The residuals from linearity are presented in Fig. 25, where $\langle E_{\rm rec} \rangle$ [GeV]$= (\langle E_{\rm vis} \rangle$ [MIPs]$-u)/v$, with u and v parameters given in Table 9. The deviations from linearity are smaller than 1%.

The width of the energy sum distribution obtained using the Novosibirsk fit is shown in Fig. 26 as a function of the beam momentum. The simulation predicts a smaller width than observed in data. The e^+ energy resolution is displayed in Fig. 27. The simulation predicts a better energy resolution than observed. The observed difference between data and simulation provides an upper limit to additional systematic effects on the resolution, which are not included in the simulation. Taking the difference in quadrature, the effects are less than 3%, in agreement with earlier measurements [12].

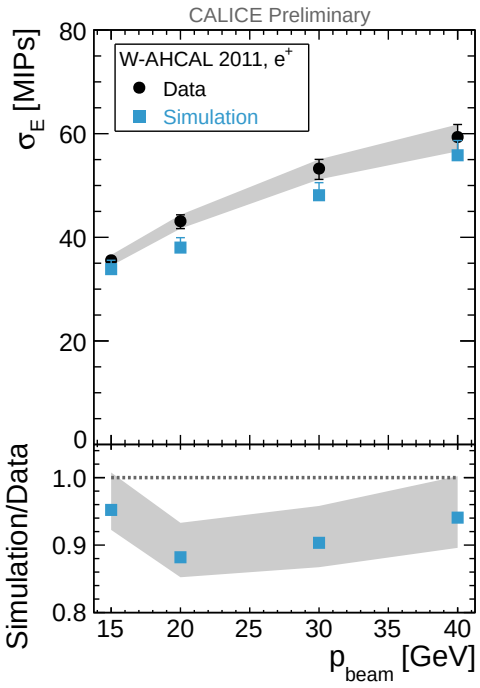

Figure 26: Width of the energy sum distribution (σ_E) for e^+ events as a function of the beam momentum. Data are compared to the simulation. The grey band shows the overall uncertainty.

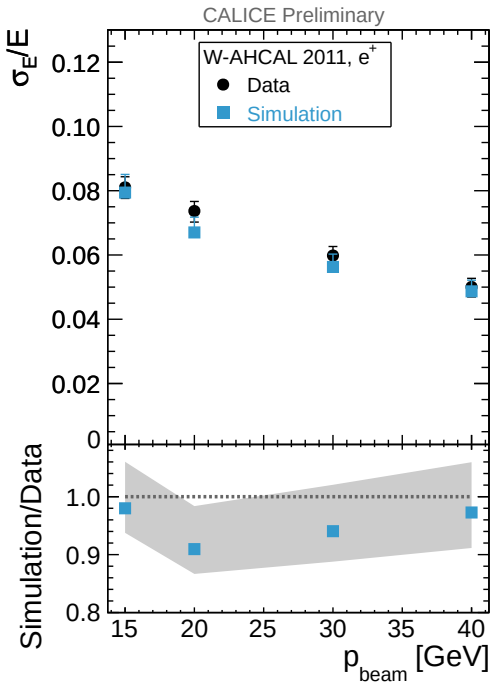

Figure 27: Energy resolution for e^+ events: comparison of data with simulation. The grey band shows the overall uncertainty.

In summary, given the large uncertainties, the electromagnetic data agrees with the simulation for the response, linearity and for longitudinal profiles. Due to the dense material, the effect of single cell calibration uncertainties is particularly large for electromagnetic data at the analysed energies, which results in a less precise validation of the simulation with electrons, compared to the low energy data [2] or to the case with the steel absorbers. However, the effect of the single calibration uncertainties is expected to be reduced for hadron showers, which have a smaller energy density per tile.

6. Selection of hadron data

The list of runs selected for the hadron analysis is given in Appendix A.2.

The first level of particle identification is based on two Cherenkov threshold counters installed upstream the W-AHCAL prototype. The purities of the obtained hadron-event samples were estimated based on a calibration measurement of the counters and taking into account the expected particle content of the respective mixed-hadron beams. A detailed description of the Cherenkov pre-selection strategy and results can be found elsewhere [18]. Remaining muon contamination is rejected by requesting that the layer of the primary interaction, identified using the algorithm defined in [21], is in any of the first 3 calorimeter layers. The energy sum distribution of 80 GeV π^+ before and after applying this cut is shown in Fig. 28.

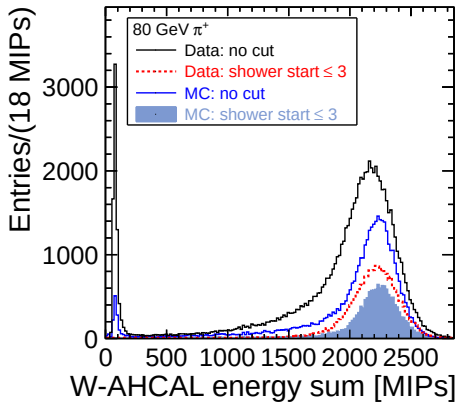

Figure 28: Energy sum distribution of 80 GeV π^+ in data and in Monte Carlo, before and after requesting that the shower start should be in the first 3 calorimeter layers.

7. Analysis of the $\pi^\pm$ data

The $\pi^\pm$ events are selected as described in Section 6. The purities of the event samples selected based on the Cherenkov threshold counters are better than 94% [18], as indicated in Appendix A.2.

In the following, comparisons with Monte Carlo are shown for the calorimeter response and for variables describing the longitudinal and the lateral shower development.

7.1 Calorimeter response

The average visible energy deposited in the calorimeter by $\pi^\pm$ induced showers is shown as a function of beam momentum in Fig. 29. The data are compared to the selected GEANT4 physics lists. As discussed in section 4.8, π^- runs show on average a higher (up to 5%) response than π^+ runs, whereas the Monte Carlo is very similar for the two particle types.

A good agreement between data and QGSP_BERT_HP and FTFP_BERT_HP is observed for π^+. This result should be compared to the corresponding Fig. 31 of [2]. In both cases the QGSP_BERT_HP simulation of the detector response matches the data very well. This also shows that after calibration, the hadronic energy scales of the 2010 and 2011 data taking periods agree. For π^-, the disagreement between data and QGSP_BERT_HP is at the level of 3% to 4%, or even more for beam momenta smaller than 20 GeV, while for the FTFP_BERT_HP the disagreement is at the level of about 4% for all momenta, but within experimental uncertainties. The highest disagreement is observed for QGSP_BIC_HP, at the level of 10%.

The results of the linear fit are given in Table 10. Both statistical (stat) and systematic (sys) uncertainties, obtained as described in Section 5.3, but using the corresponding systematic uncertainty, are indicated for the fit parameters. The slopes are similar for data and Monte Carlo (within the uncertainties), while large uncertainties are observed for the offsets.

The fact that the considered simulation models predict different slopes and offsets for π^+ and for π^- is due to the different fit ranges used for the π^+ (from 25 to 100 GeV) and for the π^- data (from 15 to 100 GeV). When

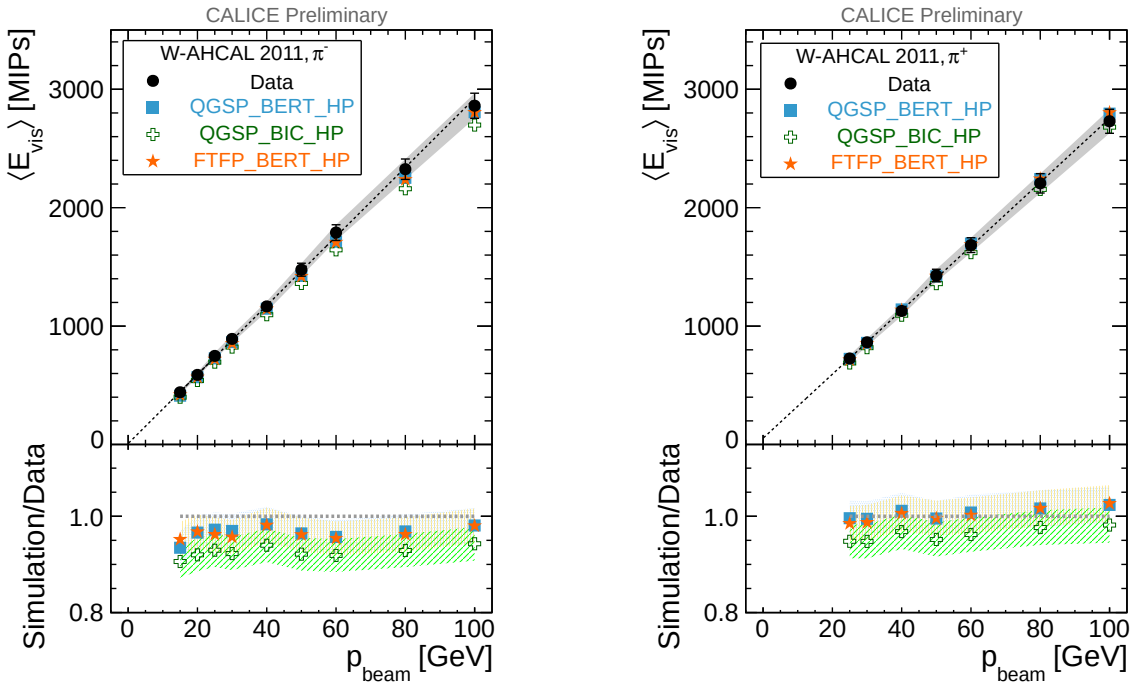

Figure 29: Average visible energy as a function of the beam momentum for π^- (left) and π^+ (right) induced showers. The data are compared with the selected GEANT4 *physics lists. The grey band shows the overall uncertainty. The dotted line indicates a fit with the function $\langle E_{\text{vis}} \rangle = u + v \cdot p_{\text{beam}}$. In the lower part of the figures, the ratios between the simulation and the data are shown. The bands show the overall uncertainty.*

Table 10: Fit parameters of the dependence of the mean $\pi^{\pm}$ visible energy on the beam momentum. The π^+ data corresponds to beam momenta from 25 to 100 GeV, whereas the π^- data corresponds to momenta from 15 to 100 GeV. Both statistical (stat) and systematic (sys) uncertainties are indicated for the fit parameters.

Particle		u [MIPs]	v [MIPs/GeV]
π^+	Data	$63.15 \pm 1.17\ (\text{stat}) \pm 73.91\ (\text{sys})$	$26.92 \pm 0.02\ (\text{stat}) \pm 1.48\ (\text{sys})$
	QGSP_BERT_HP	$34.33 \pm 1.29\ (\text{stat}) \pm 44.29\ (\text{sys})$	$27.66 \pm 0.02\ (\text{stat}) \pm 0.97\ (\text{sys})$
	QGSP_BIC_HP	$20.90 \pm 1.91\ (\text{stat}) \pm 29.89\ (\text{sys})$	$26.68 \pm 0.04\ (\text{stat}) \pm 0.80\ (\text{sys})$
	FTFP_BERT_HP	$19.11 \pm 2.00\ (\text{stat}) \pm 29.62\ (\text{sys})$	$27.84 \pm 0.05\ (\text{stat}) \pm 0.84\ (\text{sys})$
π^-	Data	$7.91 \pm 0.63\ (\text{stat}) \pm 33.14\ (\text{sys})$	$29.26 \pm 0.02\ (\text{stat}) \pm 0.88\ (\text{sys})$
	QGSP_BERT_HP	$8.44 \pm 0.92\ (\text{stat}) \pm 21.43\ (\text{sys})$	$28.27 \pm 0.02\ (\text{stat}) \pm 0.57\ (\text{sys})$
	QGSP_BIC_HP	$-10.85 \pm 0.41\ (\text{stat}) \pm 14.86\ (\text{sys})$	$27.41 \pm 0.02\ (\text{stat}) \pm 0.55\ (\text{sys})$
	FTFP_BERT_HP	$9.31 \pm 1.70\ (\text{stat}) \pm 23.65\ (\text{sys})$	$28.15 \pm 0.04\ (\text{stat}) \pm 0.56\ (\text{sys})$

fitting the same beam momenta range, from 25 to 100 GeV, for both π^- and for π^+ data, the fit results are quite similar, for a given physics list.

The deviation from linearity is presented in Fig. 30, where $\langle E_{\text{rec}} \rangle\,[\text{GeV}] = (\langle E_{\text{vis}}\,[\text{MIPs}] - u)/v$, with u and v parameters being given in Table 10. Large deviations are observed for π^- at energies below 20 GeV, which are also predicted by the simulation, while the π^+ response is linear.

For the width of the energy sum distributions obtained with a Gaussian fit as indicated in Fig. 9 and shown in Fig. 31, all Monte Carlo models predict systematically lower values than observed, in both π^- and π^+ data. The energy resolution for $\pi^{\pm}$ data is presented in Fig. 32. On average, the Monte Carlo simulations overestimate the energy resolution.

No energy resolution fits are applied due to the restricted analysed energy range (from 15 to 100 GeV). In order to obtain reliable fit parameters, a wider energy range is needed. For combining the data analysed in this paper with the low energy data [2], a common data selection needs to be developed, which is beyond the

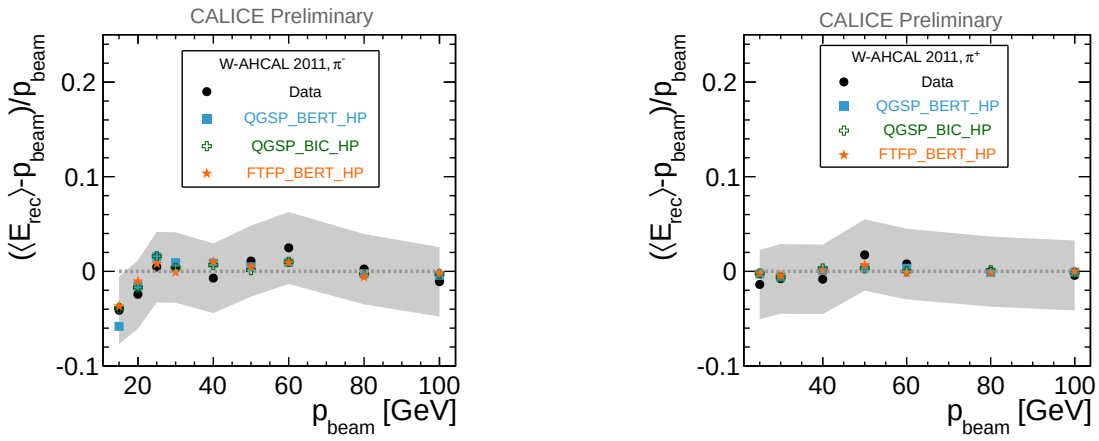

Figure 30: Deviations from linearity for the W-AHCAL 2011 π^- (left) and π^+ (right) data. The data are compared with the selected GEANT4 *physics lists. The grey band shows the overall uncertainty.*

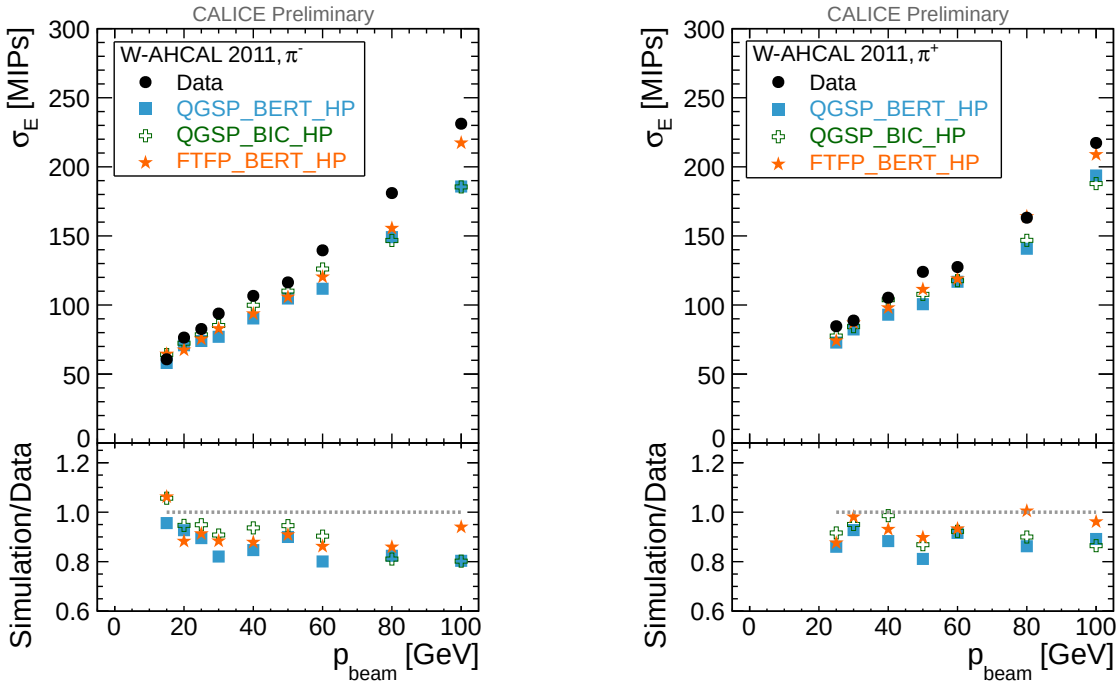

Figure 31: Width of the energy sum distributions as a function of the beam momentum for π^- (left) and π^+ (right) induced showers. The data are compared with the selected GEANT4 *physics lists. The width is obtained using a Gaussian fit in the central region containing 80% of the statistics. In the lower part of the figures, the ratios between simulation and data are shown.*

scope of this paper. Such a selection is non-trivial due to the muon contamination: the existing track algorithms are confirmed to work only for energies $E \geq 10$ GeV. The lower the energy of the incoming particle, the more difficult it is to distinguish between muons and hadrons. In order to include higher energies for the energy resolution measurement, it is necessary to measure the leakage with the Tail Catcher and Muon Tracker, and a corresponding analysis is ongoing [22].

A comparison of the energy sum distributions with the selected GEANT4 models is shown in Fig. 33 for π^+ and for π^-, for two beam momenta. The shapes agree well. However, the π^- energies in data are higher than π^+, while in the simulation no significant difference is observed between π^- and π^+.

The levelling off of the relative resolution at higher energies is predicted in the simulation and indicates that leakage starts to play a role, as one can also deduce from the tail in the energy distribution, Fig. 33 (c and d).

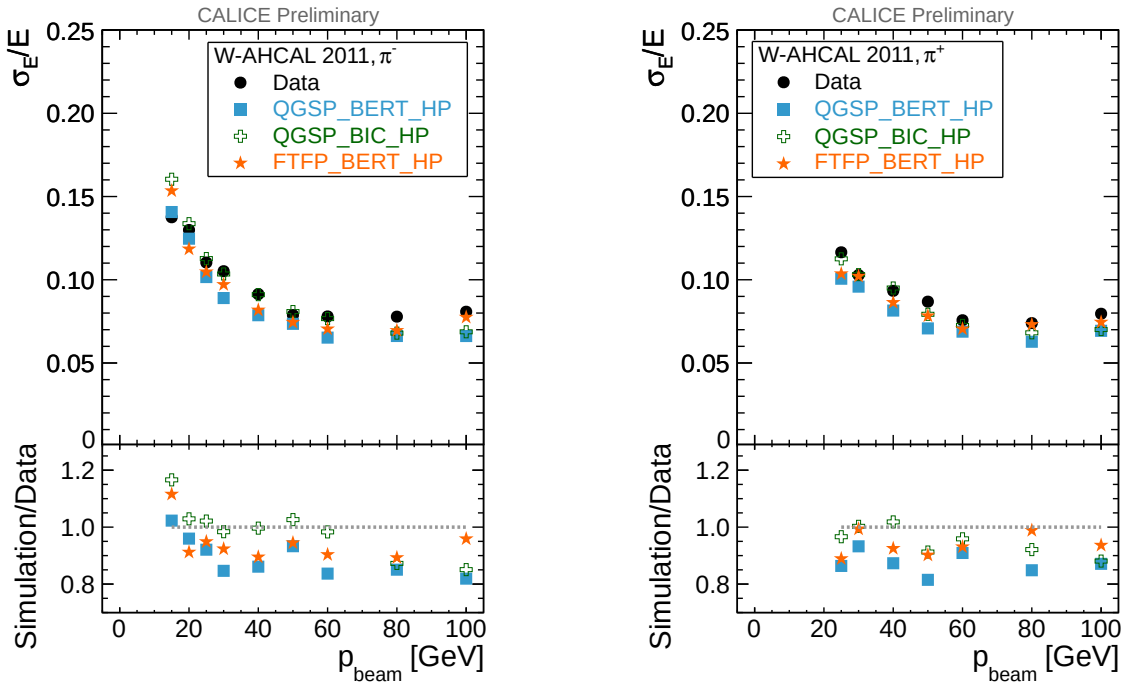

Figure 32: Energy resolution for π^- (left) and π^+ (right) induced showers. The data are compared with the selected GEANT4 *physics lists. In the lower part of the figures, the ratios between the simulation and the data are shown.*

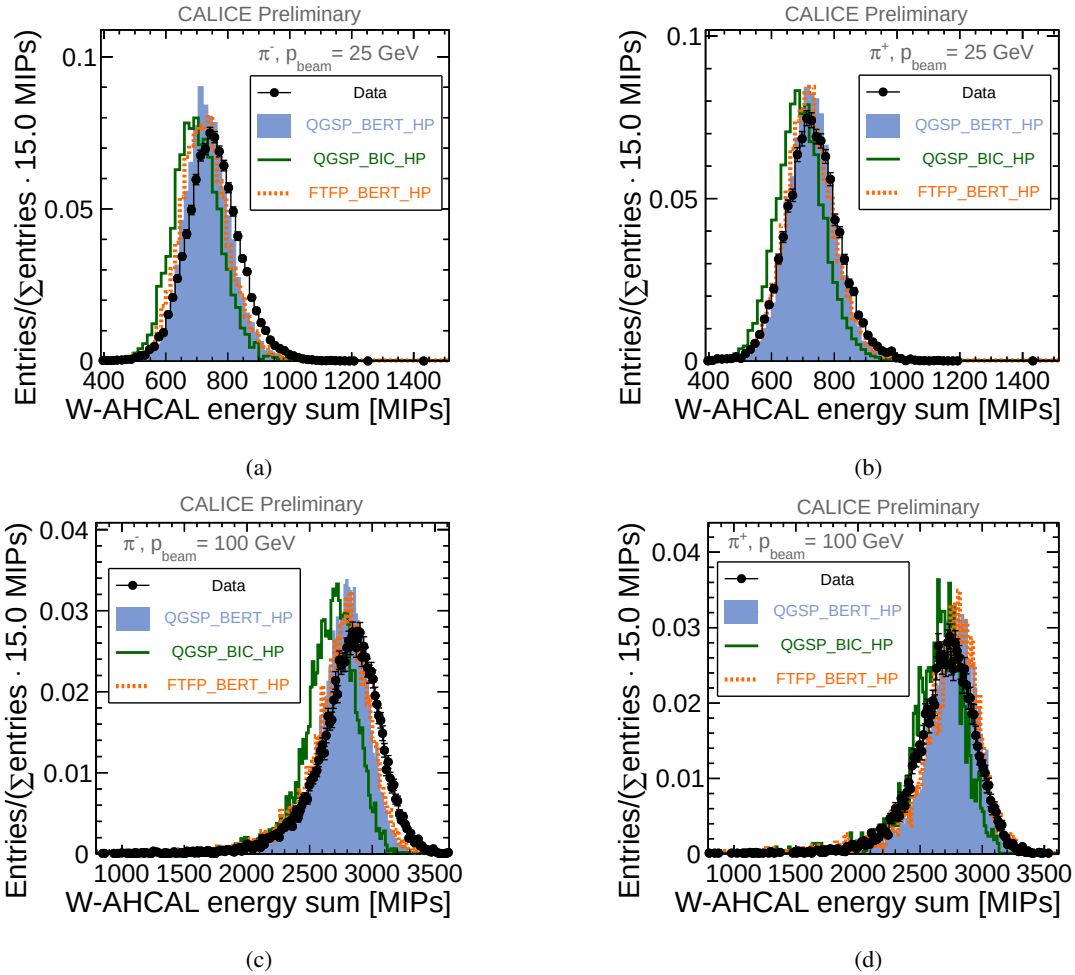

Figure 33: Energy sum distributions for 25 GeV (top) and 100 GeV (bottom) π^- (left) and π^+ (right). The data are compared with the selected GEANT4 *physics lists.*

7.2 Spatial development

In order to judge the quality of the simulation concerning the spatial development of hadronic showers, comparisons of data with Monte Carlo were also done for variables which describe the shower development along the z-axis (longitudinally) and in the (x, y) plane (transversely).

The shower shapes are shown for all considered physics lists, and for two beam momenta, 25 and 100 GeV.

7.2.1 Longitudinal shower development

The high granularity of the CALICE W-AHCAL enables the measurement of the longitudinal profile of hadron showers from the shower start, i.e. the calorimeter layer in which the primary interaction took place. This has the advantage that the statistical fluctuations of the shower start can be disentangled from the intrinsic longitudinal shower development. In addition, the layer-to-layer fluctuations due to calibration uncertainties are smeared out.

Therefore the longitudinal profiles are presented relative to the measured shower start, expressed in nuclear interaction lengths λ_{I}, where one calorimeter layer corresponds to 0.13 λ_{I} [2]. The layer in which the shower started is identified with the clustering algorithm[6] described in [11] and used also for the analysis of the Fe-AHCAL data [23]. The cluster that is nearest (in z) to the origin of the incoming particle is considered the shower start cluster. The shower start point is defined as the first point on the main principal axis within the cluster, and the shower start layer is the layer nearest (in z) to this point.

For the measurement of the longitudinal profiles, only events with a shower starting in layer 3 or later are considered. This is done in order to ensure that the selected incoming hadrons generate a shower only after they reach the calorimeter. The systematic uncertainties due to layer-by-layer fluctuations of the calorimeter response are estimated as follows:

- Profiles for showers starting in the W-AHCAL layers 3, 4, 5, ..., 16 are considered (14 profiles in total);
- The energy deposition in layer i from shower start, from each of these profiles, is filled in a histogram (35 histograms in total). The error on the mean of the histogram i is considered to be the systematic uncertainty on the energy measurement in layer i from shower start.

With this method, some bins in the tails are not covered by the 14 profiles. For example, the profile for showers starting in layer 3 (4) has 36 (35) bins, and so on.

A comparison of the longitudinal profile in data and Monte Carlo for 25 GeV and 100 GeV π^+ is shown in Fig. 34. In the lower part of the figures the ratio of simulation to data is presented, together with the systematic uncertainties band estimated with the method described above. At 25 GeV, the best description (within the uncertainties) is given by QGSP_BERT_HP, with a tendency to overestimate the energy deposition in the first part of the shower. This tendency increases with energy, as it can be seen for the 100 GeV case. An opposite behaviour, of underestimating the energy depositions in the first part of the shower, is observed for FTFP_BERT_HP.

The shower development along the z-axis can also be described by the centre-of-gravity in z, expressed in mm, indicating the energy-weighted z-position of the shower in the laboratory frame, in which the W-AHCAL front plane is placed at $z = 308$ mm. Distributions of this variable for 25 GeV $\pi^{\pm}$ are displayed in Fig. 35. In the lower part of the same figure, the average centre-of-gravity in z is shown as a function of the beam momentum. For this integrated variable, the level of agreement between data and the QGSP-models (QGSP_BERT_HP and QGSP_BIC_HP) is very similar for π^+ and for π^-, the deviations being at the level of 2% or better. For FTFP_BERT_HP slightly larger deviations, of the order of 3–4% are observed.

[6] A comparison of the different methods to obtain the shower start layer is presented in Appendix A.3.

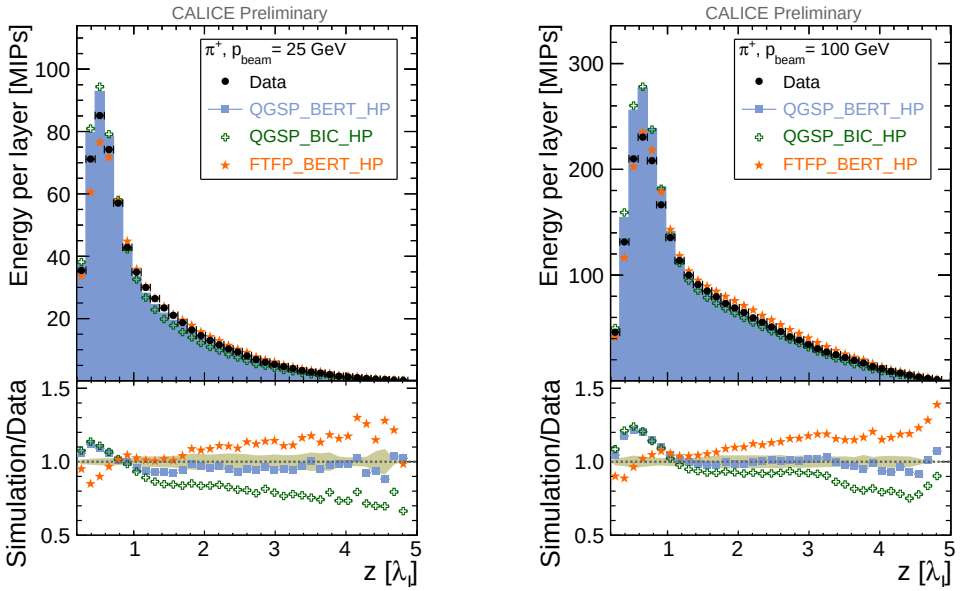

(a) (b)

Figure 34: Longitudinal profiles from shower start for 25 GeV (a) and 100 GeV π^+ (b). In the lower part of the figures, the ratio between the GEANT4 *physics lists and data is shown. The grey band indicates the systematic uncertainties on data.*

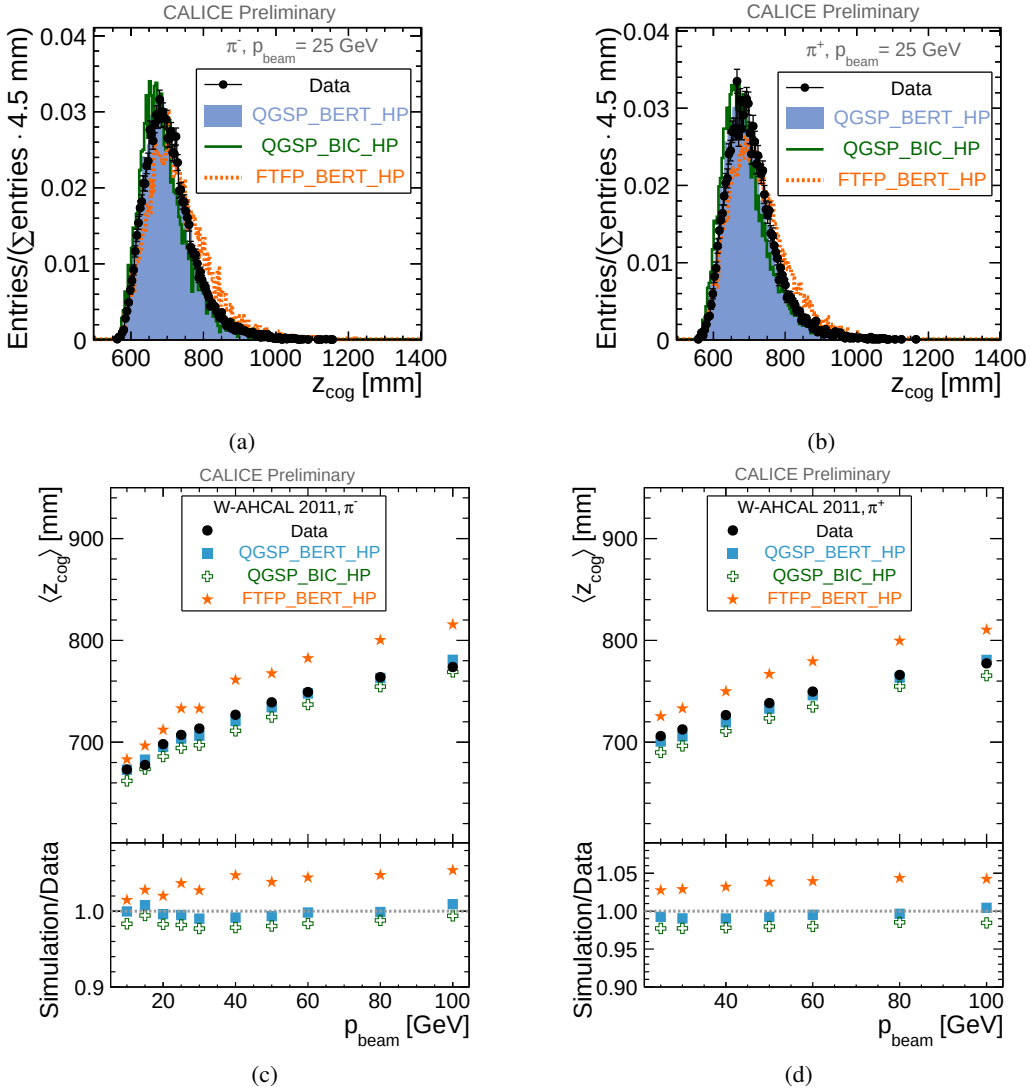

(a) (b)

(c) (d)

Figure 35: Centre-of-gravity in z for 25 GeV π^- (a) and π^+ (b). Dependence of the average centre-of-gravity in z on the beam momentum for π^- (c) and for π^+ (d). The data are compared with the GEANT4 *physics lists.*

7.2.2 Radial shower development

The radial profile is given by the distribution of the energy density (i.e., energy per square centimetre) as a function of the radial distance to the calorimeter centre, defined as:

$$r_i = \sqrt{(x_i - x_{\mathrm{cog}})^2 + (y_i - y_{\mathrm{cog}})^2}, \tag{7.1}$$

where x_i (y_i) is the x (y) position of the cell i, E_i the cell energy, and x_{cog} (y_{cog}) are the centre-of-gravities in x and y:

$$x_{\mathrm{cog}} = \frac{\sum_i E_i \cdot x_i}{\sum_i E_i} \text{ and } y_{\mathrm{cog}} = \frac{\sum_i E_i \cdot y_i}{\sum_i E_i}. \tag{7.2}$$

In order to homogenise the detector geometry, the physical W-AHCAL cells are divided into virtual cells of 1 cm^2. The energy of the incoming particle is assumed to be deposited uniformly inside these cells. More details can be found in [11, pg. 80-82]. The bin width of the x-axis is given by the dimension of the smallest W-AHCAL tile, i.e. 3×3 cm^2.

Unlike in the case of longitudinal profiles, where each bin corresponds to an individual detector layer, the bin content of the radial profiles corresponds to a sum over all layers and many tiles. We therefore do not assign bin-to-bin systematic uncertainties.

An example of a radial profile is displayed in Fig. 36 for π^+ of two beam momenta. At both momenta, the Monte Carlo simulations predict a higher density in the core of the shower than observed. However, FTFP_BERT_HP shows an energy-dependent behaviour in the tail description, the best agreement with data being observed at 100 GeV.

To further study the shower development in the radial direction, an energy weighted shower radius was defined :

$$R = \frac{\sum_i E_i \cdot r_i}{\sum_i E_i}, \tag{7.3}$$

where E_i the cell energy, and r_i is defined in equation 7.1. Distributions of the energy weighted shower radius are shown in Fig. 37 (a, b) for 25 and 100 GeV π^+. The mean shower radius is shown as a function of beam momentum in Fig. 37 (c, d). The best agreement is observed for FTFP_BERT_HP, at the level of 90% or better.

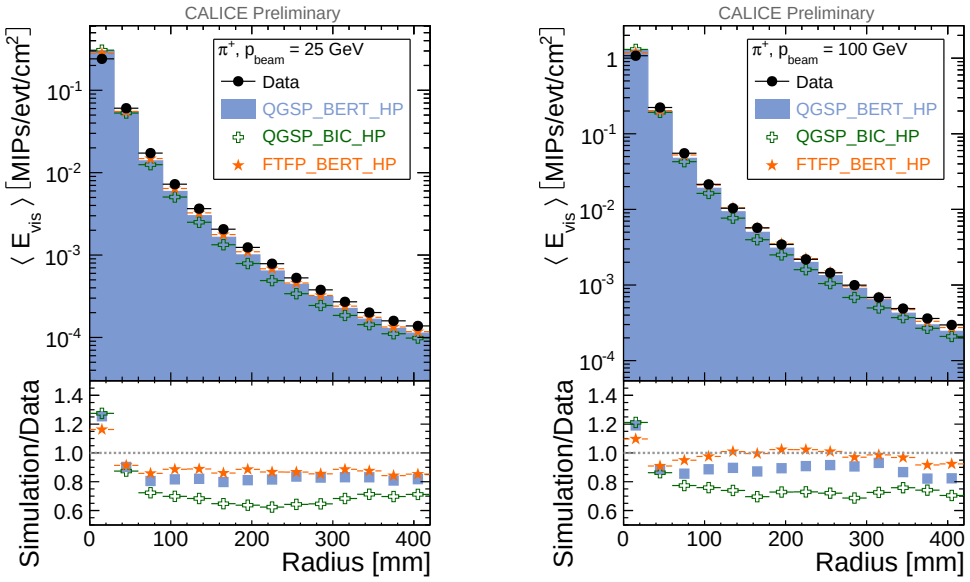

(a) (b)

Figure 36: The radial profile of 25 GeV π^+ (a) and 100 GeV π^+ (b). The data are compared with the GEANT4 *physics lists.*

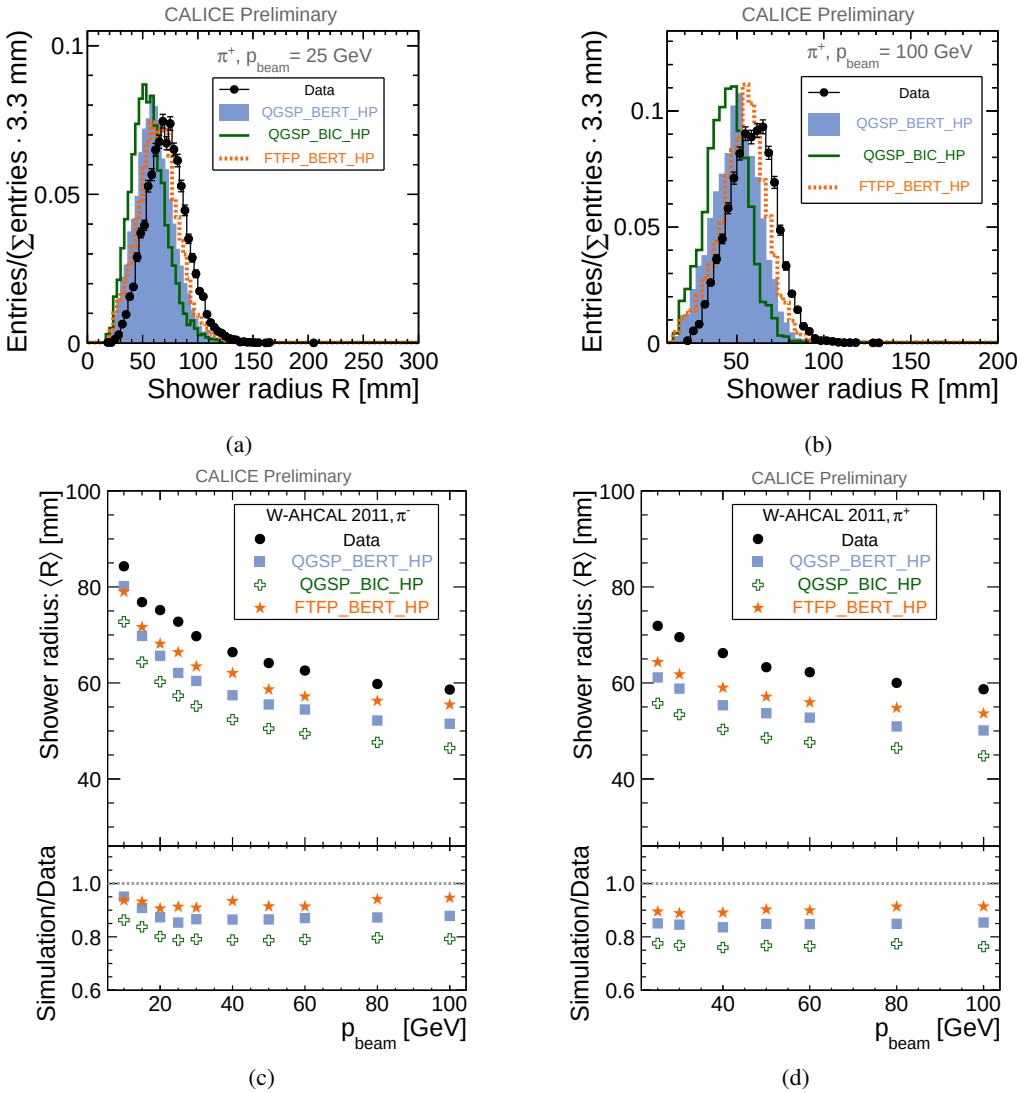

(a) (b)

(c) (d)

Figure 37: Distribution of the energy weighted shower radius for 25 GeV π^+ (a) and 100 GeV π^+ (b). Dependence of the mean shower radius as a function of the beam momentum for π^- (c) and π^+ (d). The data are compared with the GEANT4 *physics lists.*

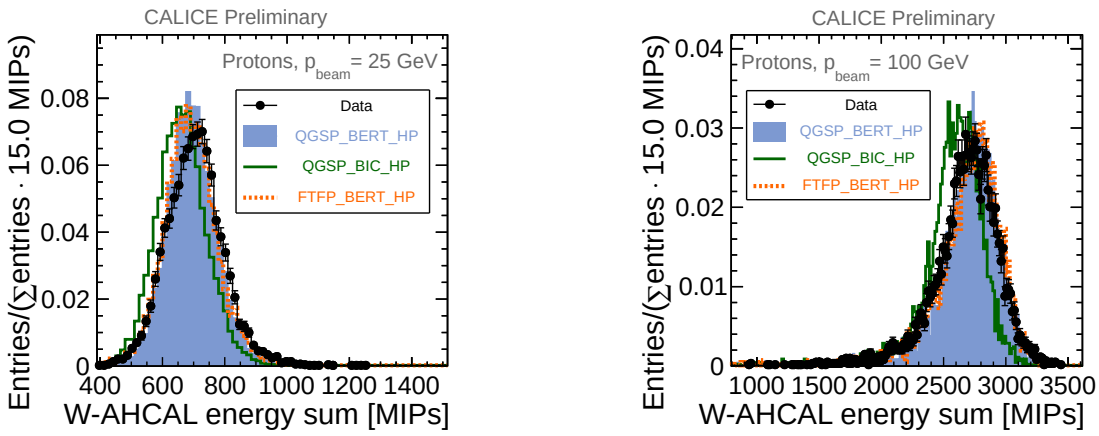

Figure 38: Distribution of the W-AHCAL energy sum for 25 GeV (left) and 100 GeV protons (right). The data are compared with the GEANT4 *physics lists.*

Table 11: Fit parameters of the dependence of the mean visible energy on the proton beam momentum. Both statistical (stat) and systematic (sys) uncertainties are indicated for the fit parameters.

	u [MIPs]	v [MIPs/GeV]
Data	22.98 ± 1.86 (stat) ± 156.49 (sys)	27.16 ± 0.03 (stat) ± 1.63 (sys)
QGSP_BERT_HP	-7.07 ± 1.26 (stat) ± 21.92(sys)	27.84 ± 0.02 (stat) ± 1.11 (sys)
QGSP_BIC_HP	-5.67 ± 1.54 (stat) ± 71.10 (sys	26.41 ± 0.03 (stat) ± 1.06 (sys)
FTFP_BERT_HP	-12.45 ± 1.94 (stat) ± 27.51 (sys)	27.87 ± 0.04 (stat) ± 0.84 (sys)

8. Analysis of the proton data

The proton events are selected as described in Section 6. The purities of the event samples selected based on Cherenkov threshold counters are better than 85% [18], as indicated in Appendix A.2. Similarly to the pion analysis, comparisons to the Monte Carlo simulations are shown for the calorimeter response, and for variables describing the longitudinal and lateral shower development.

8.1 Calorimeter response

The energy sum distributions for 25 and 100 GeV protons are shown in Fig. 38 and compared to the selected GEANT4 physics lists. The average visible energy deposited in the calorimeter by protons induced showers is shown as a function of beam momentum in Fig. 39. The agreement between data and the Bertini simulation models is good for all analysed energies, as can be seen in the lower part of the figure, while QGSP_BIC_HP underestimates the energy, but within experimental uncertainties.

The results of the linear fit are given in Table 11. Both statistical (stat) and systematic (sys) uncertainties, obtained as described in Section 5.3, are indicated for the fit parameters. The deviation from linearity is presented in Fig. 40, where $\langle E_{\text{rec}} \rangle$ [GeV] $= (\langle E_{\text{vis}}$ [MIPs] $- u)/v$, with u and v parameters being given in Table 11. The proton response is linear within the uncertainties.

For the width of the energy sum distributions, shown in Fig. 41, the Monte Carlo models predict lower values than observed. The energy resolution for the proton data is presented in Fig. 42. In general, the Monte Carlo simulations overestimate the energy resolution.

8.2 Proton/π^+ ratio

For a non-compensating calorimeter ($e/h > 1$, where e/h represents the ratio of the detector response for electrons to that of hadrons), it is expected that the energy deposited by π^+-induced showers is on average larger than the energy of protons ($E_{\pi^+} > E_{\text{protons}}$). This is due to the fact that the baryon number conservation favours the production of leading baryons, such that π^0 ($\rightarrow \gamma$) production is, on average, smaller in proton-induced showers.

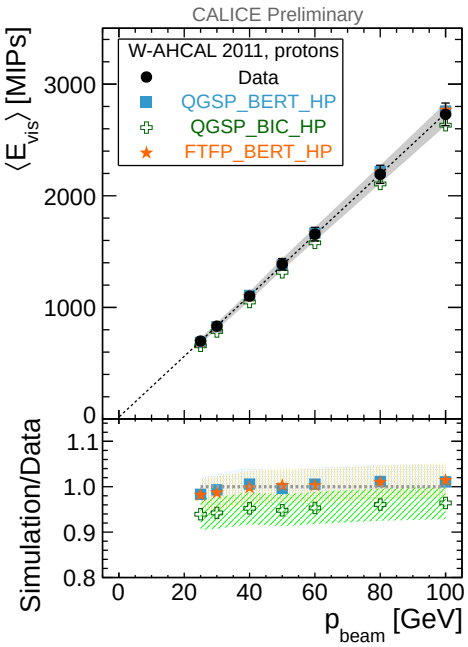

Figure 39: Dependence of the mean proton energy on the beam momentum. The mean visible energy $\langle E_{vis} \rangle$ is given by the mean of a Gaussian fit in the central region containing 80% of the statistics. The dotted line indicates a fit with the function $\langle E_{\mathrm{vis}} \rangle = u + v \cdot p_{\mathrm{beam}}$. The grey band shows the overall uncertainty. In the lower part of the figure, the ratios between simulation and data are shown. The bands correspond to the 5% uncertainty on the energy scale in Monte Carlo.

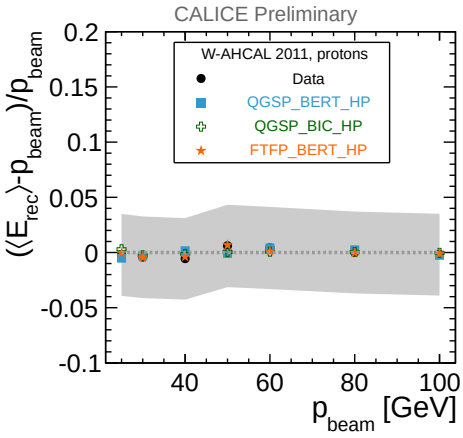

Figure 40: Deviations from linearity. The grey band shows the overall uncertainty. The data are compared with the GEANT4 *physics lists.*

This was observed for the CALICE Fe-AHCAL (Fig. 43). This holds also for the W-AHCAL (Fig. 44), but the effect is reduced, confirming the previous observation [2] that the W-AHCAL is close to compensation (see also section 10).

8.3 Longitudinal and radial shower development

The longitudinal profiles for 25 and 100 GeV protons are presented in Fig. 45 and compared to the selected GEANT4 physics list. In the lower part of the figures the ratio of simulation to data is presented. The grey band indicates the systematic uncertainties, estimated as explained in section 7.2.1. As in the pion case, at 25 GeV the best description (within the uncertainties) is given by QGSP_BERT_HP, with a tendency to overestimate the energy deposition in the first part of the shower. The QGSP-based simulations are similar, while FTFP_BERT_HP underestimates the energy in the first part of the showers, and overestimates it in the last part. At 100 GeV however, QGSP_BIC_HP is better in describing the energy depositions per layer, especially in the first part of the shower.

The distributions of the centre-of-gravity in z are shown for 25 and 100 GeV protons in Fig. 46 (a and b). The average mean centre-of-gravity in z, $\langle z_{\mathrm{cog}} \rangle$, is shown as a function of the beam momentum in Fig. 46 (c). A good agreement is observed between data and the QGSP-based models, while the agreement between data and the FTFP_BERT_HP model is at the level of about 95%.

The radial profiles for 25 and 100 GeV protons are shown in Fig. 47. As in the pion case, the simulation models predict a higher density in the core of the shower than observed.

The distributions of the energy weighted shower radius, defined in equation 7.3, are shown in Fig. 48 for 25 and 100 GeV protons. The agreement between data and Monte Carlo is constant for all analysed energies, the best being for FTFP_BERT_HP, at the level of 95%.

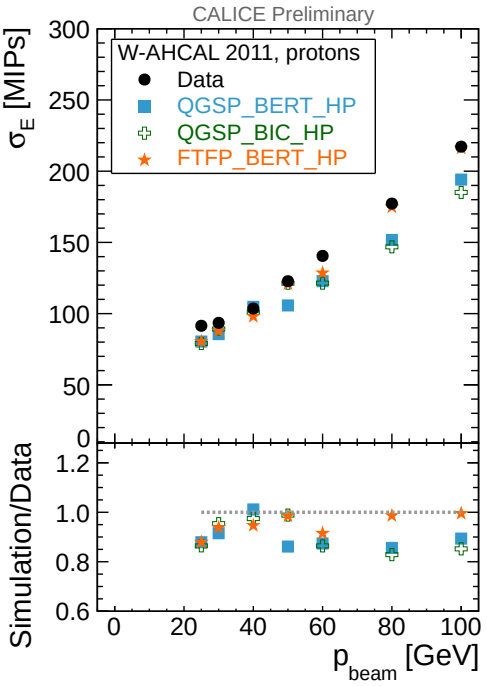

Figure 41: Dependence of the width of the proton energy sum distributions on the beam momentum. The data are compared with the GEANT4 *physics lists. The width is obtained with a Gaussian fit in the central region containing 80% of the statistics. In the lower part of the figure, the ratios between simulation and data are shown.*

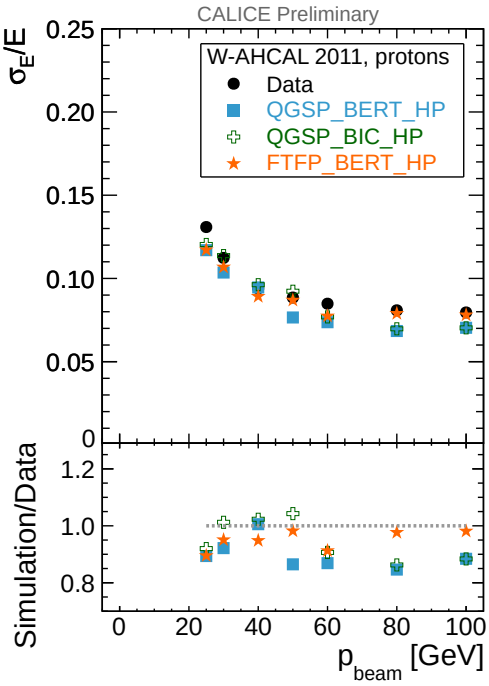

Figure 42: Energy resolution for protons. The data are compared with the GEANT4 *physics lists. In the lower part of the figure, the ratios between simulation and data are shown.*

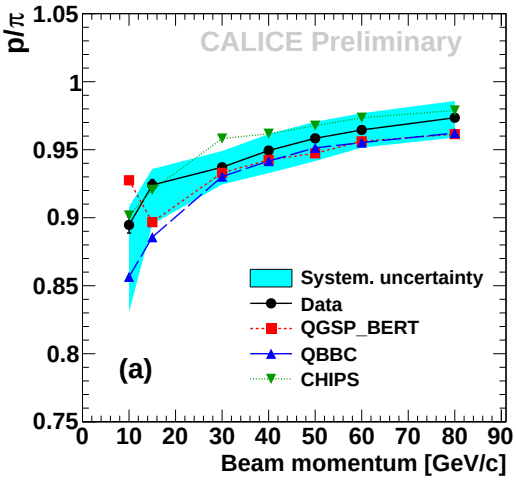

Figure 43: Ratio between proton and π^+ energy depositions in the CALICE Fe-AHCAL (from [24]). The data are compared with the GEANT4 *physics lists.*

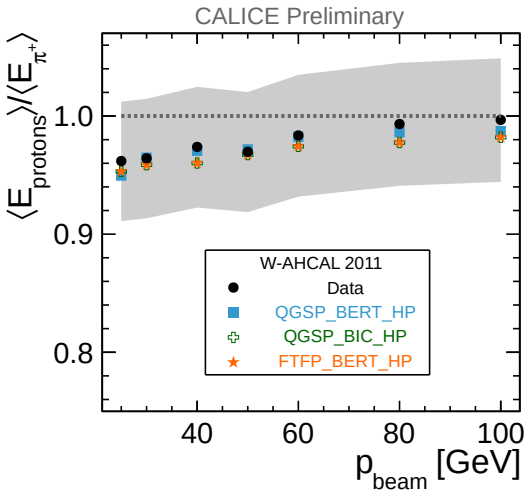

Figure 44: Ratio between proton and π^+ energy depositions in the CALICE W-AHCAL. The data are compared with the GEANT4 *physics lists. The grey band shows the overall uncertainty.*

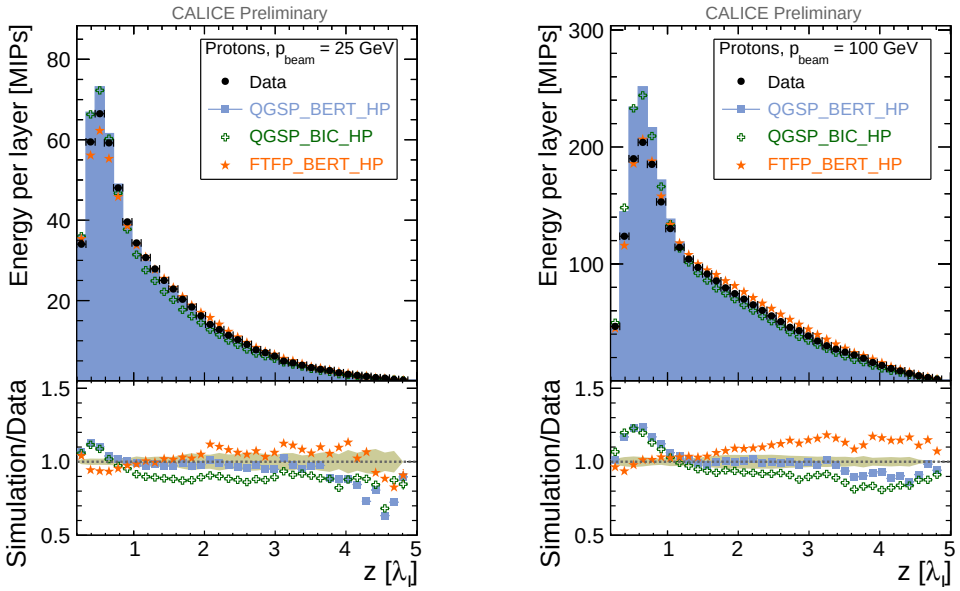

(a) (b)

Figure 45: Longitudinal profiles from shower start for 25 GeV (a) and 100 GeV (b) protons. In the lower part of the figures, the ratio between the GEANT4 *physics lists and data is shown. The grey band indicates the systematic uncertainties on data.*

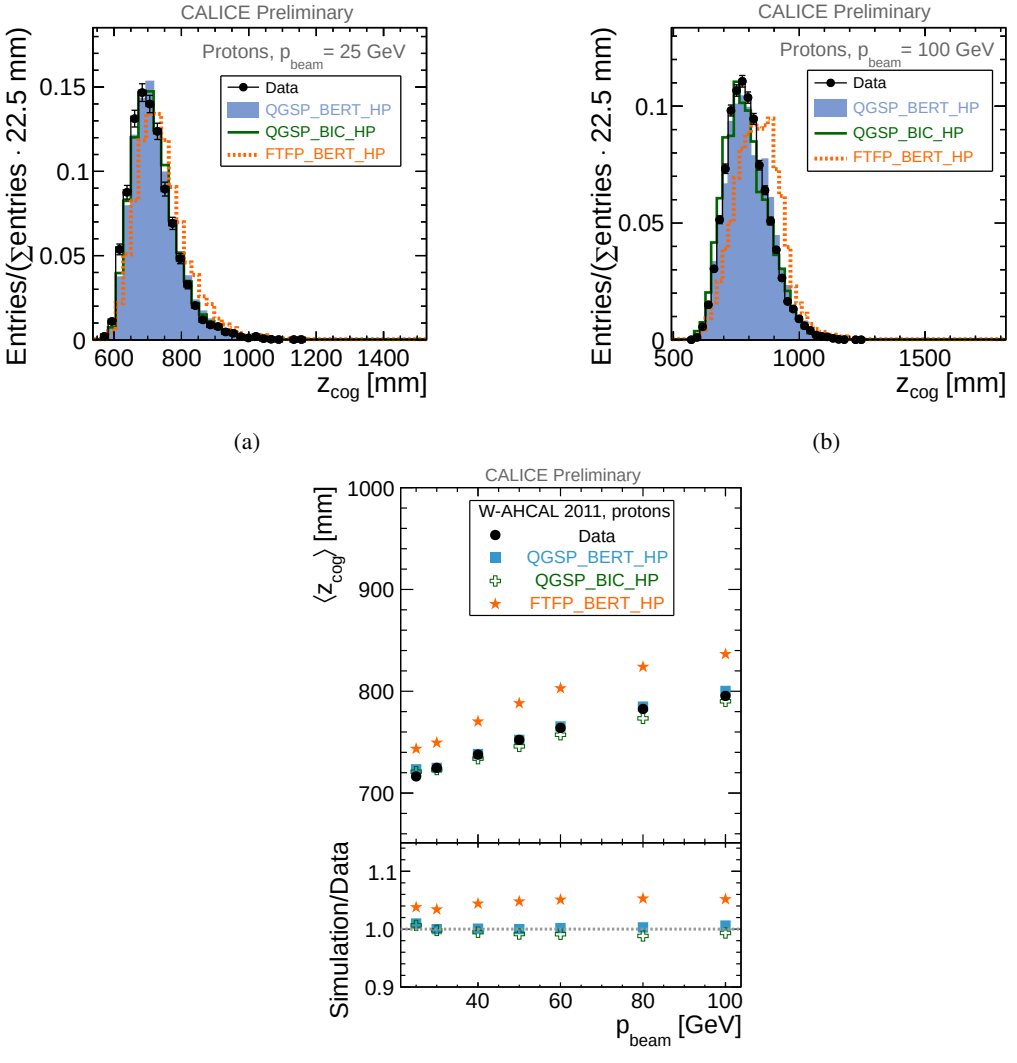

(a) (b)

(c)

Figure 46: Distribution of the centre-of-gravity in z for 25 GeV (a) and 100 GeV protons (b). Dependence of mean centre-of-gravity in z on the beam momentum (c). The data are compared with the GEANT4 *physics lists.*

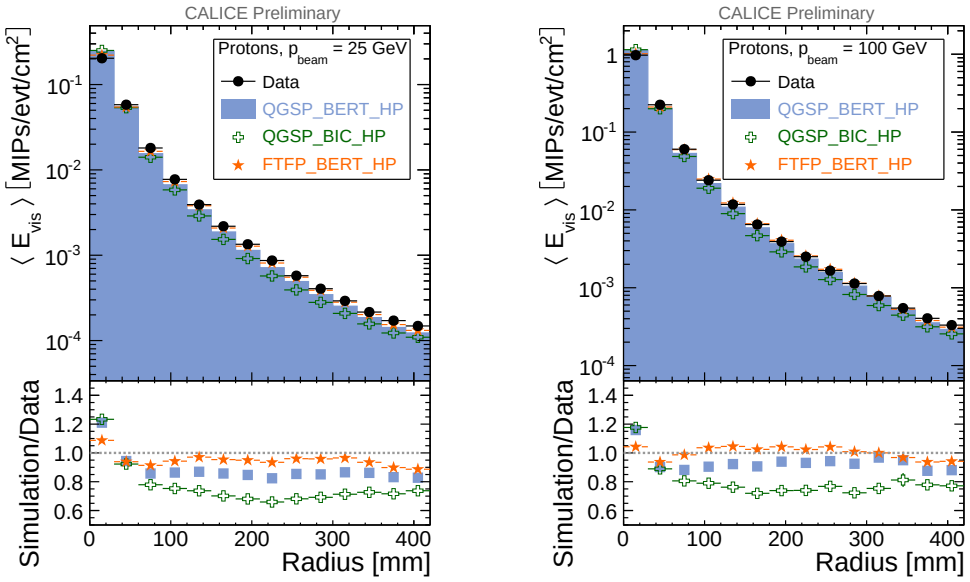

(a) (b)

Figure 47: Radial profile for 25 GeV (a) and 100 GeV protons (b). The data are compared with the GEANT4 *physics lists. In the lower part of the figure, the ratios between simulation and data are shown.*

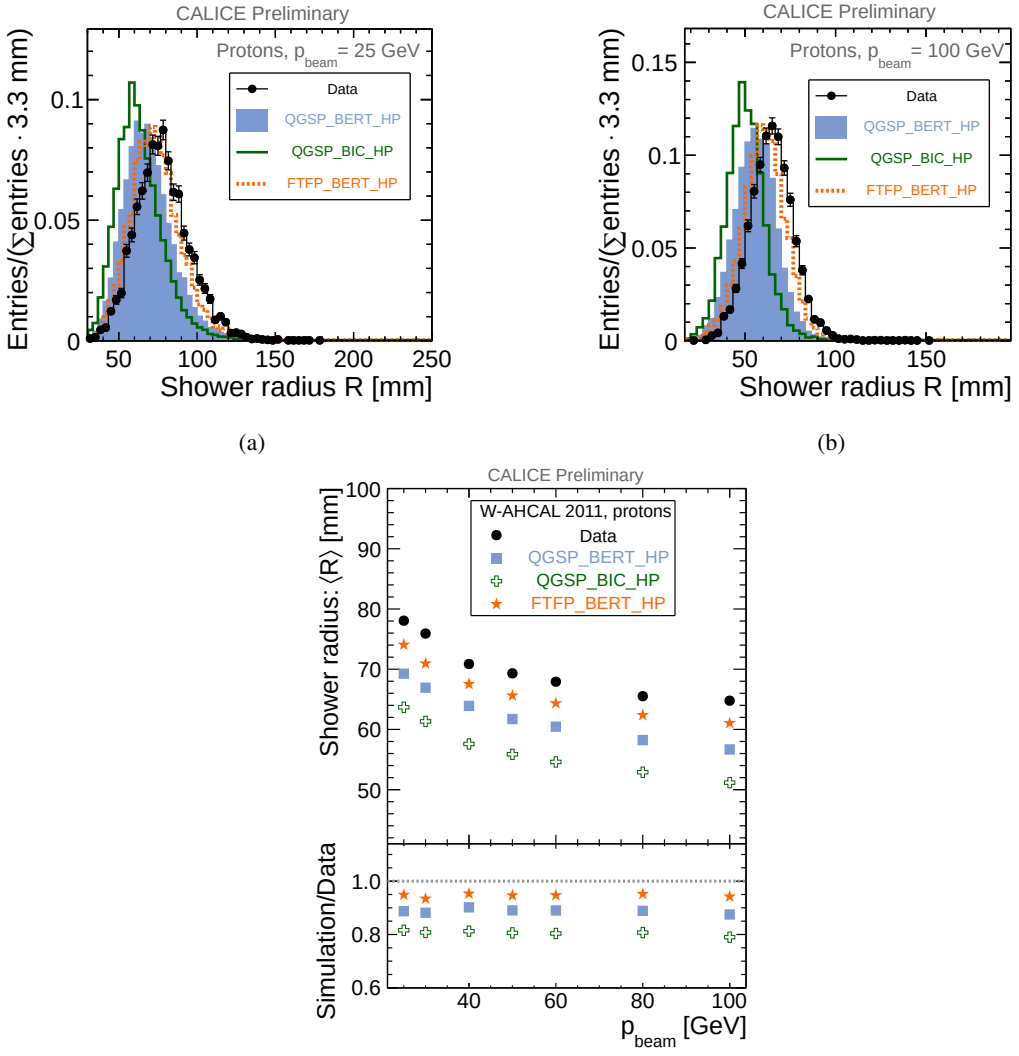

(a) (b)

(c)

Figure 48: Shower radius distribution for 25 GeV (a) and 100 GeV protons (b). Dependence of mean shower radius on the beam momentum (c). The data are compared with the GEANT4 *physics lists.*

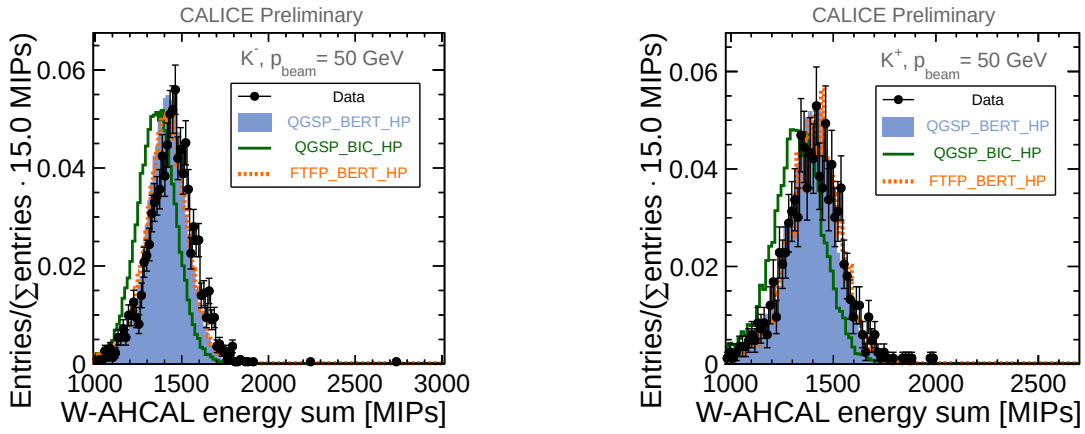

Figure 49: Energy sum distributions for 50 GeV K^- (left) and K^+ (right). The data are compared with the GEANT4 *physics lists.*

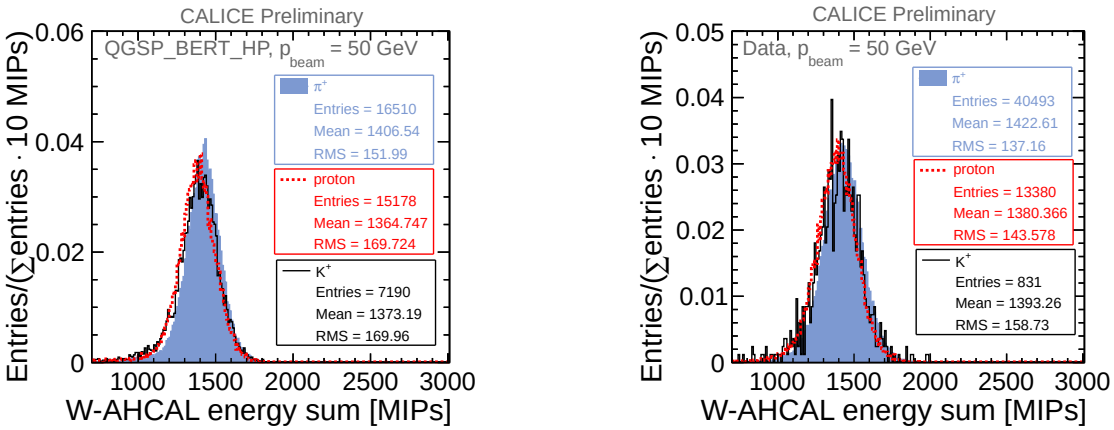

Figure 50: Energy sum distributions for the analysed hadrons with a beam momentum of 50 GeV. The QGSP_BERT_HP (left) and the data (right) are shown.

9. Analysis of the $K^{\pm}$ data

In the hadron beam, a relatively small fraction of events are expected to have kaon-induced showers. Data corresponding to beam momenta of 50 and 60 GeV were selected since in this case the purities of the event samples selected based on Cherenkov threshold counters are better than 82% [18], as indicated in Appendix A.2.

The energy sum distributions for 50 GeV K^- and K^+ are compared to the simulation in Fig. 49. A good agreement with the Bertini models is observed for K^+, whereas K^- has a higher energy in data (as for the π^- case). QGSP_BIC_HP predicts systematically lower energies than observed.

When comparing the calorimeter response to the different hadrons at a given beam momentum, it is observed that the response is very similar, with QGSP_BERT_HP predicting a slightly lower energy for protons and for K^+ compared to the π^+ case, as shown in Fig. 50. As discussed in section 4.7, no correction for possible contamination from other hadrons is applied in data.

9.1 K^- vs. K^+ in simulation

In Fig. 51 the total cross sections for K^-n and K^+n collisions are shown as a function of laboratory beam momentum. There is a difference between K^- and K^+, which decreases with increasing beam momentum. Due to the slightly different cross sections in the two cases, it is expected to see a small difference in the energy deposited in the calorimeter. This is indeed observed at generator level (i.e., pure GEANT4 energy deposition, no detector effects included), as presented in Fig. 52. However, the expected differences are about 1% and unfortunately below our experimental sensitivity.

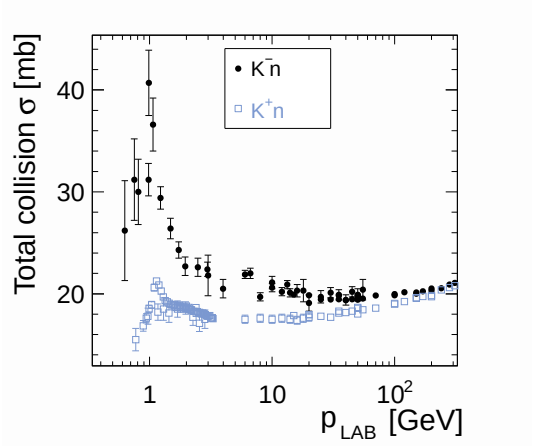

Figure 51: Total cross sections for K^-n and K^+n collisions as a function of laboratory beam momentum [25].

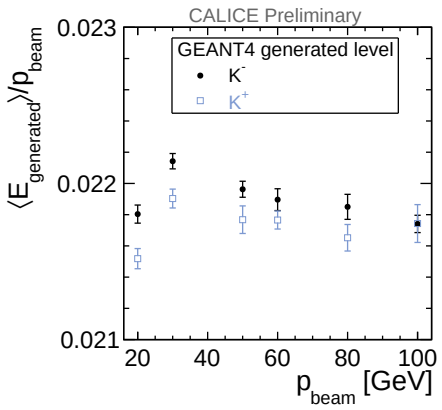

Figure 52: Mean visible energy of $K^\pm$ divided by the beam momentum, as a function of the beam momentum, for events generated using the QGSP_BERT_HP physics list. The mean energy is obtained with a Gaussian fit in the central region.

9.2 Longitudinal and radial shower development

The longitudinal shower profile from shower start is shown in Fig. 53 for 60 GeV K^+. The ratio between simulation and data is shown in the lower part of the figure. The grey band indicates the systematic uncertainties, estimated as explained in section 7.2.1. The best agreement is for the FTFP_BERT_HP model, whereas the QGSP-based models overestimate the energy depositions in the first part of the shower.

The centre-of-gravity in z is presented in Fig. 54. The QGSP-based models are very similar, and close to data, while the FTFP_BERT_HP predicts slightly higher values than observed. The radial profile for 60 GeV K^+ is shown in Fig. 55 (left). The simulation predicts a larger energy density in the shower core, but the agreement of Bertini models with data improves as the radius increases. The shower radius distributions for 60 GeV K^+ are displayed in Fig. 55 (right). The best agreement is obtained for FTFP_BERT_HP.

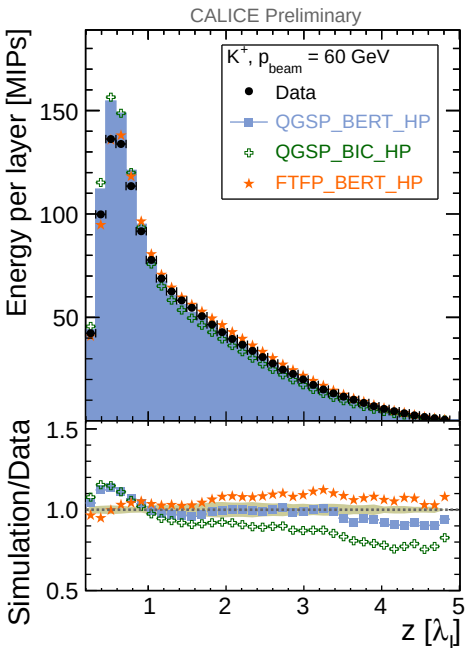

Figure 53: Longitudinal profile from shower start for 60 GeV K^+. The data are compared with the GEANT4 *physics lists. In the lower part of the figure, the ratios between simulation and data are shown. The grey band indicates the systematic uncertainties on data.*

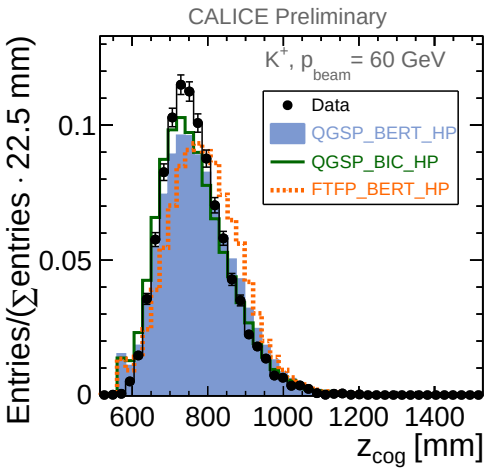

Figure 54: The distribution of the centre-of-gravity in z (right) for 60 GeV K^+. The data are compared with the GEANT4 *physics lists.*

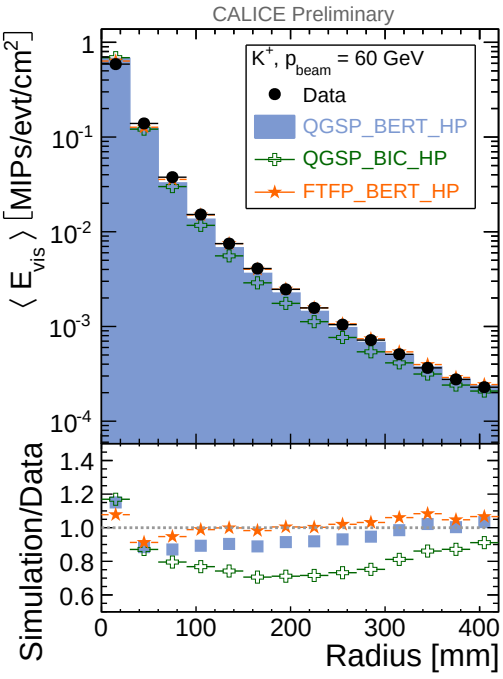

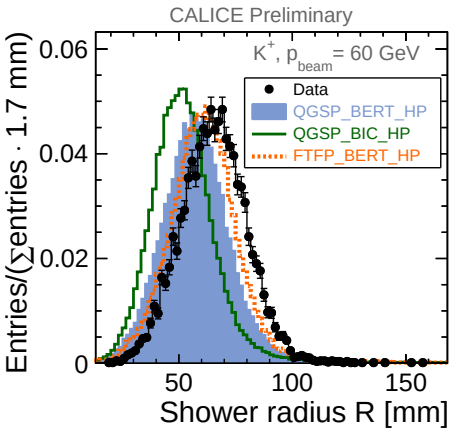

Figure 55: Radial profile (left) and shower radius distribution (right) for 60 GeV K^+. Data are compared to the GEANT4 *physics lists.*

10. Comparison of the response for different particle types

For the comparison of the calorimeter response to different particle types, the data corresponding to the positively charged particles are chosen, because this minimises the variations with time, as discussed in section 4.8 and shown in Fig. 10. Pions and protons are from the same runs, and also the positron data were taken with a minimal change of beam settings and close-by in time.

The calorimeter response to π^+, protons, K^+ and positrons is compared in Fig. 56 for data (left) and for simulation (right). The upper part of the figures shows the reconstructed energy as a function of the available energy[7]. The lower part of the figures shows the residuals from the linear fit of the experimental π^+ data. The deviations from the fit are better than $\pm 2\%$ for π and protons, and somewhat worse for e^+. These values differ from the residuals from the linear fit applied to each particle type separately (shown in figure 25 for e^+ and in figure 40 for protons), because the parameters of the π^+ fit are used for all particles.

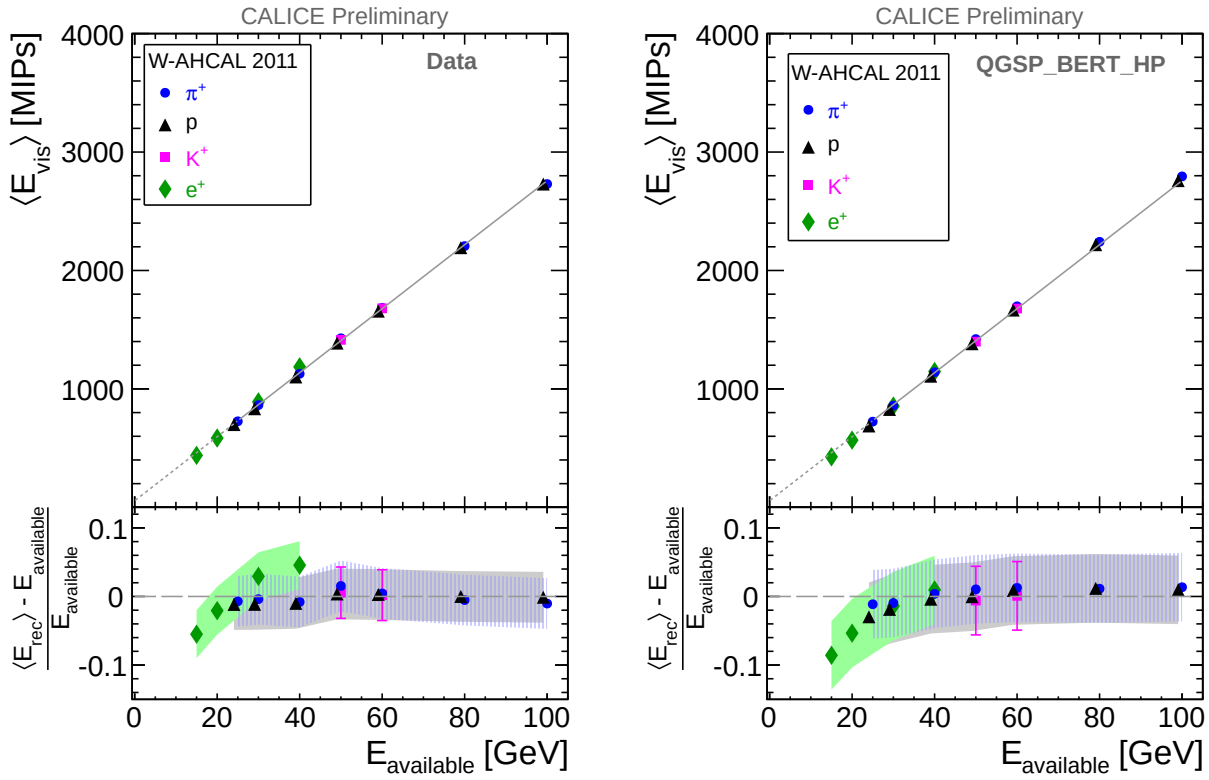

Figure 56: The response of the CALICE W-AHCAL to different particles as a function of the available energy for data (left) and for QGSP_BERT_HP (right). The grey line indicates a fit of the π^+ experimental data with the function $\langle E_{\mathrm{vis}} \rangle = u + v \cdot p_{\mathrm{beam}}$. The dotted grey line indicates the extrapolation of the line to zero. The lower part of the figures shows the residuals from this fit, where $\langle E_{\mathrm{rec}} \rangle [\mathrm{GeV}] = (\langle E_{\mathrm{vis}} \rangle [\mathrm{MIPs}] - u)/v$. The bands show the overall uncertainties (Table 5).

The dominant systematic uncertainty, which is due to variations of the detector response with time (Table 5) affects the comparison between electromagnetic and hadronic showers. As explained in section 8.2 the calorimeter response to π^+ is slightly higher than the response to protons. However, the effect is reduced with increasing beam momentum. In conclusion, given the overall uncertainties in the measurements, the detector response is similar for all particle types. In GEANT4 simulations, shown in Fig. 56 (right), a close to compensation behaviour is expected, and this is confirmed by the measurements. The same observation was already made with the W-AHCAL for positrons, pions and protons in the energy range from 2 to 10 GeV [2].

[7] The available energy is defined as $E_{\mathrm{available}} = \sqrt{m^2_{\mathrm{proton}} + p^2_{\mathrm{beam}}}$ for protons, and as $E_{\mathrm{available}} = \sqrt{m^2_{\mathrm{particle}} + p^2_{\mathrm{beam}}}$ for the other particles, where m is the particle mass, and p_{beam} the beam momentum.

11. Summary and conclusions

The data taken with the CALICE W-AHCAL prototype in 2011 at CERN SPS, containing a mixture of $e^{\pm}$, $\pi^{\pm}$, proton, $K^{\pm}$ and $\mu^{\pm}$ events, are presented. To reduce leakage effects, the analysis is restricted to particles with beam momenta from 15 to 100 GeV, and to early starting showers. The measured calorimeter response, resolution, and longitudinal and lateral profiles are compared with the following GEANT4 physics lists: QGSP_BERT_HP, QGSP_BIC_HP and FTFP_BERT_HP. In general the data show a good detailed agreement with the simulations.

The data sample was collected over two separate running periods (June/July and September/October 2011) and shows larger variations of the detector response ($\pm 3.1\%$ for hadrons), after temperature correction, than observed in earlier test beam campaigns, which is reflected in a larger systematic uncertainty. In addition, systematic uncertainties due to the MIP scaling factor, and to the imprecise knowledge of the saturation scaling factor were estimated, resulting in a total uncertainty of $^{+3.6\%}_{-4.1\%}$ for 40 GeV e^+, and of $\pm 3.7\%$ for hadrons. Within this uncertainty, the response to positive and negative particles is consistent.

The agreement between the e^+ data and the simulation is good for response and linearity, and satisfactory for the longitudinal profiles. Due to the dense absorber material (a calorimeter layer corresponds to about 2.8 radiation lengths X_0), in electromagnetic showers a smaller number of cells contain energy deposits, compared to the case of the hadron showers. In addition, a significant part of the energy of the whole electromagnetic shower is deposited in only one cell. As a consequence, the uncertainties on the single cell calibration factors have a considerable impact.

When comparing the positive hadron data with the GEANT4 physics lists, similar conclusions can be drawn for π^+, for protons and for K^+:

- In the case of calorimeter response to hadrons, overall the best agreement between data and simulation is obtained for the Bertini-based physics lists (QGSP_BERT_HP and FTFP_BERT_HP), at the level of 98% or better. The response is the same, within systematic uncertainties, for positrons, pions, kaons and protons, in agreement with GEANT4 based predictions.

- All considered simulation models predict better hadron energy resolutions than observed in the data. No energy resolution fits are applied due to the restricted analysed energy range (from 15 to 100 GeV). In order to obtain reliable fit parameters, a wider energy range is needed. For combining the data analysed in this paper with the low energy data [2], a common data selection needs to be developed, which is beyond the scope of this paper.

- In the case of longitudinal profiles from shower start, the QGSP-based models (QGSP_BERT_HP and QGSP_BIC_HP) overestimate the energy depositions at the beginning of the shower. Overall, the best agreement is obtained with QGSP_BERT_HP in the case of pions, and with FTFP_BERT_HP in the case of protons and kaons. For the radial profiles, the simulation models predict a higher density in the core of the shower than observed. The best agreement is observed for FTFP_BERT_HP, at the level of 90% or better.

12. Outlook

Considering the different aspects of the data quality which resulted from the present analysis, the following improvements are envisaged for a future system:

- Usage of SiPMs with reduced temperature sensitivity and of an improved temperature measurement system;

- Improved test bench characterisation of the photo-sensors for a precise measurement of the saturation level and of the cross-talk factor;

- Taking high statistics of muon calibration runs at stable temperatures, and with large scintillator triggers, covering as much as possible of the whole detector, such that all channels can be calibrated;

- Development of a procedure to enable the analysis of the calibrated and temperature corrected data on a short time scale, of the order of a few hours. Since usually test beams take only a few days to two weeks, getting feedback quickly is important.

A. Appendices

A.1 List of $e^{\pm}$ runs

Table 12: List of $e^{\pm}$ runs from the 2011 CALICE W-AHCAL data taking. Each run has approximately 200000 events.

p_{beam} [GeV]	Polarity	
	+	−
10		361468
15	361688, 361701	361466, 361467
20	361689, 361692	361475
25		361474
30	361702	361478
40	361687	361477

A.2 List of selected hadron runs

Table 13: List of selected π^+ runs from the 2011 CALICE W-AHCAL data taking and the corresponding sample purity, which is determined using Cherenkov counter information [18]. Each run has approximately 200000 events.

p_{beam} [GeV]	Run number	Sample purity
25	361225, 361233	100%
30	361216, 361217	100%
40	361214, 361215	100%
50	361235, 361249, 361250, 361703, 361704, 361646	98%
60	361645, 361659, 361660, 361661, 361664, 361665, 361666, 361667, 361668, 361669, 361670, 361671, 361672, 361673, 361681, 361683, 361719, 361720, 361722, 361723, 361724, 361726	100%
80	361728, 361729, 361730, 361731, 361732, 361733, 361735, 361738, 361739, 361740, 361741, 361756, 361757, 361758, 361759, 361760, 361761, 361762, 361763, 361765	100%
100	361621 361637, 361747	95%

Table 14: List of selected π^- runs from the 2011 CALICE W-AHCAL data taking and the corresponding sample purity, which is determined using Cherenkov counter information [18]. Each run has approximately 200000 events.

p_{beam} [GeV]	Run number	Sample purity
15	361470	100%
20	361255, 361257, 361263, 361264, 361469	100%
25	361269	100%
30	361267, 361270, 361271, 361472, 361473	100%
40	361253	94%
50	361273, 361373, 361375, 361415, 361479, 361480, 361481, 361482, 361483	100%
60	361354, 361356, 361357	100%
80	361351, 361376, 361400, 361401, 361416	100%
100	361341, 361352, 361353, 361404	96%

Table 15: List of selected proton runs from the 2011 CALICE W-AHCAL data taking and the corresponding sample purity, which is determined using Cherenkov counter information [18]. Each run has approximately 200000 events.

p_{beam} [GeV]	Run number	Sample purity
25	361225, 361233	86%
30 40	361216, 361217 361214, 361215	86% 85%
50	361235, 361249, 361250, 361703, 361704, 361646	100%
60	361645, 361659, 361660, 361661, 361664, 361665, 361666, 361667, 361668, 361669, 361670, 361671, 361672, 361673, 361681, 361683, 361719, 361720, 361722, 361723, 361724, 361726	100%
80	361728, 361729, 361730, 361731, 361732, 361733, 361735, 361738, 361739, 361740, 361741, 361756, 361757, 361758, 361759, 361760, 361761, 361762, 361763, 361765	100%
100	361621 361637, 361747	100%

Table 16: List of selected K^- runs from the 2011 CALICE W-AHCAL data taking and the corresponding sample purity, which is determined using Cherenkov counter information [18]. Each run has approximately 200000 events.

p_{beam} [GeV]	Run number	Sample purity
50	361479, 361480, 361481 361482, 361483,	89%
60	361354, 361356, 361357	82%

Table 17: List of selected K^+ runs from the 2011 CALICE W-AHCAL data taking and the corresponding sample purity, which is determined using Cherenkov counter information [18]. Each run has approximately 200000 events.

p_{beam} [GeV]	Run number	Sample purity
50	361646, 361703, 361704	99%
60	361645, 361659, 361660, 361661, 361664, 361665, 361666, 361667, 361668, 361669, 361670, 361671, 361672, 361673, 361681, 361683, 361719, 361720, 361722, 361723, 361724, 361726	89%

A.3 Comparison of the shower start finders

There are two software packages in the CALICE software which can be used to estimate the shower start, i.e. the calorimeter layer in which the primary interaction took place:

- The `PrimaryTrackFinder`: its purpose is to find the track corresponding to a primary particle entering the calorimeter, assuming normal incidence with respect to the calorimeter front plane and using a nearest-neighbour criterion to select one hit per layer starting from the first front plane layer and up to the found shower start layer.

  The starting layer is identified using the accumulated average energy deposited:

  $$A_i = \sum_{k=0}^{i} \frac{E_k}{i+1}, \tag{A.1}$$

  where E_k is the energy deposited in the layer k of the AHCAL. The layer i where a hadronic shower starts is then defined as the first layer for which the following criteria are fulfilled:

  $$(A_i + A_{i+1}) > \quad (6.0 + 0.1 \cdot E_{\text{beam}}/\text{GeV}) \tag{A.2}$$

  $$\text{and } (N_i + N_{i+1}) > (3.77 + 1.44 \cdot \ln(E_{\text{beam}}/\text{GeV}) + 0.5), \tag{A.3}$$

  where N_i is the number of hits in layer i.

  The above parametrisations were obtained using Fe-AHCAL Monte Carlo samples with known first interaction point, by minimising the RMS deviation of the found shower starting layer from the true one. Additional information about this finder can be found in [21]. Estimations of its quality using simulated samples are given in [26].

- The `ShowerStartCluster`: this is a nearest-neighbour algorithm developed in [11]. Cells with energies above a threshold of 2 MIPs are used as seeds for clustering. All active cells which surround the seed cell and have an energy deposit above the threshold are added to the cluster. The cluster that is nearest to the origin of the incoming particle, containing at least 6 hits, and with a total energy of at least 10 MIPs, is considered the shower start cluster. The shower start point is defined as the first point on the main principal axis within the cluster, and the shower start layer is the layer nearest (in z) to this point.

For integral variables, like the energy sum in the calorimeter, the two methods give similar results, as it can be seen in Fig. 57.

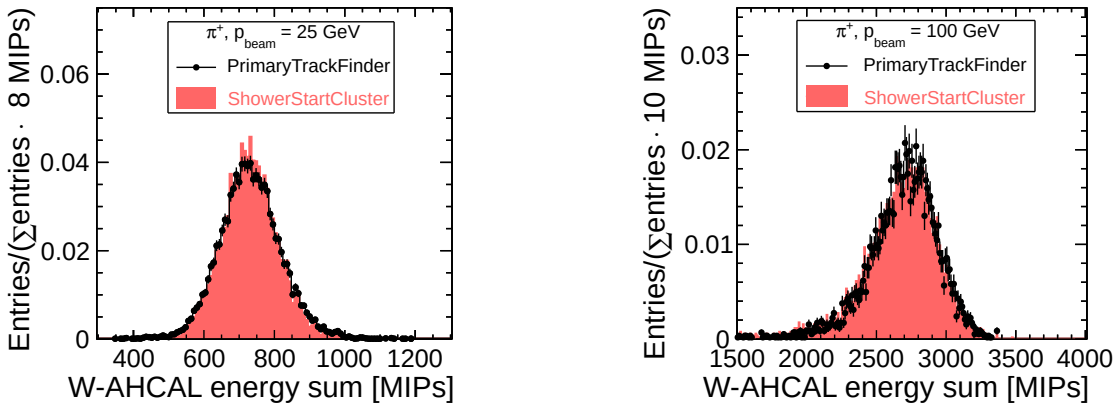

Figure 57: Energy sum distributions for 25 GeV (left) and 100 GeV (right) π^+. Two shower start finding methods are compared. Only events with showers starting in the first 3 calorimeter layers were considered.

However, the longitudinal profiles from shower start obtained with the first method showed a shift of about one layer between data and Monte Carlo for high energy pions, as visible in Fig. 58 (bottom, left). This is most

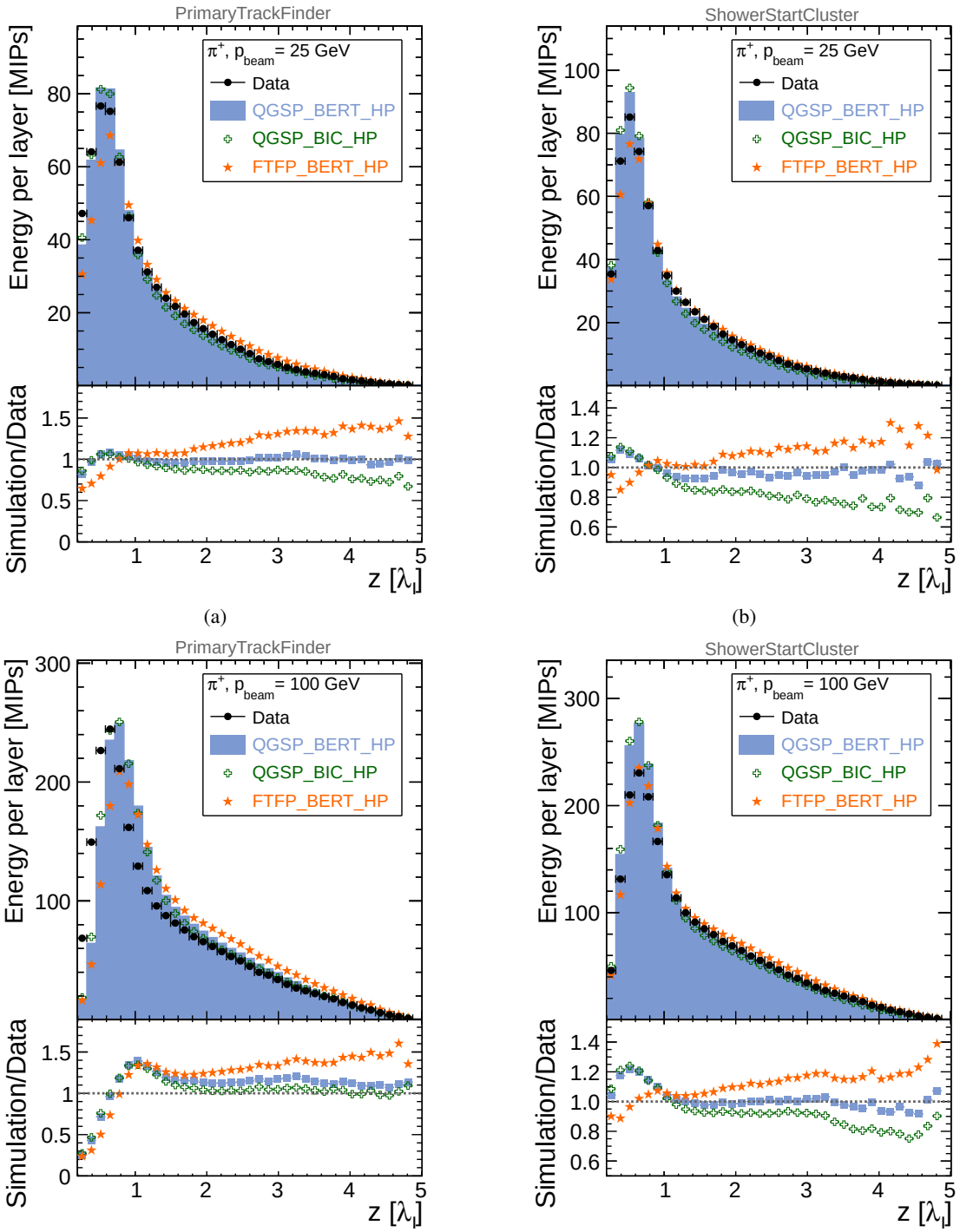

Figure 58: Longitudinal profiles with respect to the shower start layer, for 25 (top) and 100 GeV π^+ (bottom). The shower start was obtained using the `PrimaryTrackFinder` *(left) and the* `ShowerStartCluster` *(right). Only events with showers starting in the third calorimeter layer or later were considered.*

probably due to the fact that the parametrisations used for the accumulated average energy deposit and for the number of hits per layer were obtained based on simulated Fe-AHCAL data. For a more precise determination of the start of showers in the W-AHCAL with this method new parametrisations will have to be determined using W-AHCAL simulations.

References

[1] C. Adloff et al. *Construction and Commissioning of the CALICE Analog Hadron Calorimeter Prototype*. *JINST*, vol. 5 p. P05004, 2010. arXiv:1003.2662.

[2] CALICE collaboration. *Shower development of particles with momenta from 1 to 10 GeV in the CALICE Scintillator-Tungsten HCAL*. CALICE Analysis Note CAN-036, 2011.

[3] D. Dannheim, W. Klempt and E. van der Kraaij. *Beam tests with the CALICE tungsten analog hadronic calorimeter prototype*. LCD-Note-2012-002, 2012.

[4] S. Agostinelli et al. GEANT4 – A Simulation Toolkit. *Nucl. Instrum. Methods Phys. Res., Sect. A*, vol. 506(3) pp. 250–303, 2003.

[5] L. Linssen, A. Miyamoto, M. Stanitzki, and H. Weerts, eds. *Physics and Detectors at CLIC: CLIC Conceptual Design Report*. CERN, 2012. ANL-HEP-TR-12-01, CERN-2012-003, DESY 12-008, KEK Report 2011-7, arXiv:1202.5940.

[6] Mokka, a detailed GEANT4 simulation for the International Linear Collider detectors. Website: `http://ilcsoft.desy.de/portal/software_packages/mokka/`.

[7] D. Mergelkuhl and P. Andreo. *Measurement of CALICE on H8 Test Beam*. `https://edms.cern.ch/document/1151449`, 2011.

[8] CALICE collaboration. *The time structure of hadronics showers in tungsten and steel with T3B*. CALICE Analysis Note CAN-038, 2012.

[9] CALICE collaboration. *Construction and performance of a silicon photomultiplier/extruded scintillator tail-catcher and muon-tracker*. *JINST*, vol. 7 p. P04015, 2012. arXiv:1201.1653.

[10] A. Lucaci-Timoce. *Status report on the analysis of the 2011 CALICE W-AHCAL data*. LCD-Note-2013-002, 2013.

[11] B. Lutz. *Hadron showers in a highly granular calorimeter*. Ph.D. thesis, University of Hamburg, 2010. DESY-THESIS-2010-048, http://www-library.desy.de/preparch/desy/thesis/desy-thesis-10-048.pdf.

[12] C. Adloff et al. *Electromagnetic response of a highly granular hadronic calorimeter*. *JINST*, vol. 6 p. P04003, 2011. arXiv:1012.4343.

[13] R. Brun and F. Rademakers. ROOT – an object oriented data analysis framework. *Nucl. Instrum. Methods Phys. Res., Sect. A*, vol. 389(1-2) pp. 81–86, 1997.

[14] D. Dannheim, W. Klempt and A. Lucaci-Timoce. *Temperature studies of the CALICE W-HCAL with CERN 2010 data*. LCD-Note-2011-001, 2011.

[15] A. Lucaci-Timoce. *Status of tungsten analysis*. Talk at HCAL main meeting, 13th December 2011, DESY Hamburg, Germany.

[16] N. Feege. *Silicon Photomultipliers: Properties and Application in a Highly Granular Calorimeter*. Diploma thesis, DESY-THESIS-08-050, Universität Hamburg, 2008.

[17] C. Günter and J. Dietrich. *Cross-talk and calibration studies for the WHCAL testbeam*. Talk in the CALICE AHCAL main meeting, December, 2011.

[18] D. Dannheim, K. Elsener, W. Klempt, A. Lucaci-Timoce, E. van der Kraaij. *Particle identification with Cherenkov detectors in the 2011 CALICE tungsten analog hadronic calorimeter test beam at the CERN SPS*. https://cds.cern.ch/record/1545809, LCD-Note-2013-006, 2013.

[19] M. Aharrouche et al. Energy linearity and resolution of the ATLAS electromagnetic barrel calorimeter in an electron test-beam. *Nucl. Instrum. Methods Phys. Res.*, vol. A568 pp. 601–623, 2006.

[20] CALICE collaboration. *Identification of track segments in hadronic showers in the Analog Hadron Calorimeter - Algorithm and comparisons to simulations*. CALICE Analysis Note CAN-022, 2010.

[21] CALICE collaboration. *Local and global software compensation approaches: application to test beam data*. CALICE Analysis Note CAN-035, 2011.

[22] E. Sicking. Status report on the W-AHCAL + TCMT analysis. Talk in the CALICE meeting, 20th March, 2013, Hamburg, Germany.

[23] C. Adloff, et al. *Validation of GEANT4 Monte Carlo Models with a Highly Granular Scintillator-Steel Hadron Calorimeter*. 2013. arXiv:1306.3037.

[24] CALICE collaboration. *Pion and proton showers in the CALICE scintillator-steel AHCAL: comparison of global observables*. CALICE Analysis Note CAN-040, 2013.

[25] Data files and plots of cross-sections and related quantities in the 2012 Review of Particle Physics (Particle Data Group). `http://pdg.lbl.gov/2012/hadronic-xsections/`, 2012.

[26] CALICE collaboration. *Pion showers in the CALICE AHCAL prototype*. CALICE Analysis Note CAN-026, 2009.